



The Second Radio Synchrotron Background Workshop: Conference Summary and Report

J. Singal¹, N. Fornengo^{2,3}, M. Regis^{2,3}, G. Bernardi^{4,5,6}, D. Bordenave^{7,8}, E. Branchini^{9,10}, N. Cappelluti¹¹, A. Caputo^{12,13,14}, I. P. Carucci^{2,3}, J. Chluba¹⁵, A. Cuoco^{2,3}, C. DiLullo¹⁶, A. Fialkov¹⁷, C. Hale¹⁸, S. E. Harper¹⁵, S. Heston¹⁹, G. Holder²⁰, A. Kogut¹⁶, M. G. H. Krause²¹, J. P. Leahy¹⁵, S. Mittal²², R. A. Monsalve^{23,24,25}, G. Piccirilli²⁶, E. Pinetti^{27,28}, S. Recchia^{2,3}, M. Taoso³, and E. Todarello^{2,3}

¹ Department of Physics, University of Richmond, 138 UR Drive, Richmond, VA 23173, USA; jsingal@richmond.edu

² Dipartimento di Fisica, Università di Torino, via P. Giuria 1, 10125 Torino, Italy

³ Istituto Nazionale di Fisica Nucleare, Sezione di Torino, via P. Giuria 1, 10125 Torino, Italy

⁴ INAF-Istituto di Radioastronomia, via Gobetti 101, 40129, Bologna, Italy

⁵ Department of Physics and Electronics, Rhodes University, P.O. Box 94, Makhanda, 6140, South Africa

⁶ South African Radio Astronomy Observatory (SARAO), Black River Park, 2 Fir Street, Observatory, Cape Town, 7925, South Africa

⁷ Department of Astronomy, University of Virginia, 530 McCormick Road, Charlottesville, VA 22904, USA

⁸ Central Development Laboratory, National Radio Astronomy Observatory, 1180 Boxwood Estate Road, Charlottesville, VA 22903, USA

⁹ Department of Mathematics and Physics, University Roma Tre, L. San Leonardo Murialdo, 1, Rome, Italy

¹⁰ Department of Physics, University of Genoa, Via Dodecaneso 33, 16146 Genoa, Italy

¹¹ Department of Physics, University of Miami, Knight Physics Building 330, Coral Gables, FL 33146, USA

¹² Department of Particle Physics, School of Physics and Astronomy, Tel Aviv University, Chaim Levanon St. 55, Tel Aviv-Yafo, Israel

¹³ Department of Particle Physics and Astrophysics, Weizmann Institute of Science, 234 Herzl Street, POB 26, Rehovot Rehovot, Israel

¹⁴ Department of Theoretical Physics, CERN, Esplanade des Particules 1, P.O. Box 1211, Geneva 23, Switzerland

¹⁵ Jodrell Bank Centre for Astrophysics, Department of Physics & Astronomy, The University of Manchester, M13 9PL, UK

¹⁶ NASA Goddard Space Flight Center, 8800 Greenbelt Road, Greenbelt, MD 20771, USA

¹⁷ Institute of Astronomy, University of Cambridge, Madingley Road, Cambridge CB3 0HA, UK

¹⁸ Institute for Astronomy, University of Edinburgh, Blackford Hill, Edinburgh EH9 3HJ, UK

¹⁹ Department of Physics, Virginia Tech, Blacksburg, VA 24061-0435, USA

²⁰ Department of Physics, University of Illinois, 1110 West Green Street, Urbana, IL 61801, USA

²¹ Centre for Astrophysics Research, Department of Physics, Astronomy and Mathematics, University of Hertfordshire, Hatfield, Hertfordshire AL10 9AB, UK

²² Dept. of Theoretical Physics, Tata Institute of Fundamental Research, Homi Bhabha Road, Mumbai 400005, India

²³ Space Sciences Laboratory, University of California, 7 Gauss Way, Berkeley, CA 94720, USA

²⁴ School of Earth and Space Exploration, Arizona State University, 781 Terrace Mall, Tempe, AZ 85287, USA

²⁵ Facultad de Ingeniería, Universidad Católica de la Santísima Concepción, Alonso de Ribera 2850, Concepción, Chile

²⁶ Department of Physics, University of Roma Tor Vergata, Via della Ricerca Scientifica, 1 00133 Rome, Italy

²⁷ Fermi National Accelerator Laboratory, P.O. Box 500 Batavia, IL 60510, USA

²⁸ Kavli Institute for Cosmological Physics, University of Chicago, Chicago, IL 60637, USA

Received 2022 November 24; accepted 2023 February 15; published 2023 March 20

Abstract

We summarize the second radio synchrotron background workshop, which took place on 2022 June 15–17 in Barolo, Italy. This meeting was convened because available measurements of the diffuse radio zero level continue to suggest that it is several times higher than can be attributed to known Galactic and extragalactic sources and processes, rendering it the least well-understood electromagnetic background at present and a major outstanding question in astrophysics. The workshop agreed on the next priorities for investigations of this phenomenon, which include searching for evidence of the radio Sunyaev–Zel’dovich effect, carrying out cross-correlation analyses of radio emission with other tracers, and supporting the completion of the 310 MHz absolutely calibrated sky map project.

Unified Astronomy Thesaurus concepts: [Radio continuum emission \(1340\)](#); [Galactic radio sources \(571\)](#); [Extragalactic radio sources \(508\)](#); [Radio astronomy \(1338\)](#)

1. Introduction

The radio synchrotron background (RSB) is a phenomenon that has been of interest to many in the astrophysical community in recent years. Combining Absolute Radiometer for Cosmology, Astrophysics, and Diffuse Emission 2 (ARCADE 2)

measurements from 3 to 90 GHz (Fixsen et al. 2011) with several radio maps at lower frequencies from which an absolute zero level has been inferred (recently summarized in Dowell & Taylor 2018) reveals a synchrotron background brightness spectrum,

$$T_{\text{BGND}}(\nu) = 30.4 \pm 2.6 \text{ K} \left(\frac{\nu}{310 \text{ MHz}} \right)^{-2.66 \pm 0.04} + T_{\text{CMB}}, \quad (1)$$

where T_{CMB} is the frequency-independent contribution of 2.725 K due to the cosmic microwave background (CMB). This surface brightness of the radio zero level, shown in Figure 1, is several times higher than that attributable to known classes of discrete extragalactic radio sources (e.g., Hardcastle et al. 2021), which is in dramatic contrast to the observed monopole components at infrared, optical/UV, X-ray, and gamma-ray wavelengths.

In addition, various Galactic and extragalactic production mechanisms are highly constrained, due to observations of other galaxies and tracers of Galactic radio emission (e.g., Singal et al. 2015), the radio/far-infrared correlation (e.g., Ysard & Lagache 2012) and inverse-Compton implications for the X-ray background (e.g., Singal et al. 2010), effects of the presence of a radio background for H I 21 cm cosmological signals (e.g., Fialkov & Barkana 2019), and, potentially, observed arcminute-scale anisotropy constraints at gigahertz (Holder 2014) and MHz (Offringa et al. 2022) frequencies.

A second workshop on the RSB was merited, given that it touches on so many contemporary issues in astrophysics, and especially given the developments in both theory and observation that have taken place in the 5 yr since the first radio synchrotron background workshop was held in 2017 at the University of Richmond in Virginia, USA. That previous workshop has been summarized in Singal et al. (2018).

This report presents a summary of the presentations, discussions, and conclusions of the 2022 workshop for the rest of the astrophysical community. Section 2 reports the logistical details of the meeting. Section 3 gives a brief summary of the problem of the RSB. Section 4 gives a summary of individual presentations in the workshop. The overall conclusions from the various discussions are presented in Section 5.

2. Meeting Details

The organizing committee consisted of Jack Singal (University of Richmond), Marco Regis (University of Torino and INFN), and Nicolao Fornengo (University of Torino and INFN). This workshop was part of a series of Barolo Astroparticle Meetings (BAM), which are organized by the theoretical astroparticle group of the University of Torino and INFN-Torino on a semiregular basis. Participation in the workshop was by invitation of the organizing committee only,

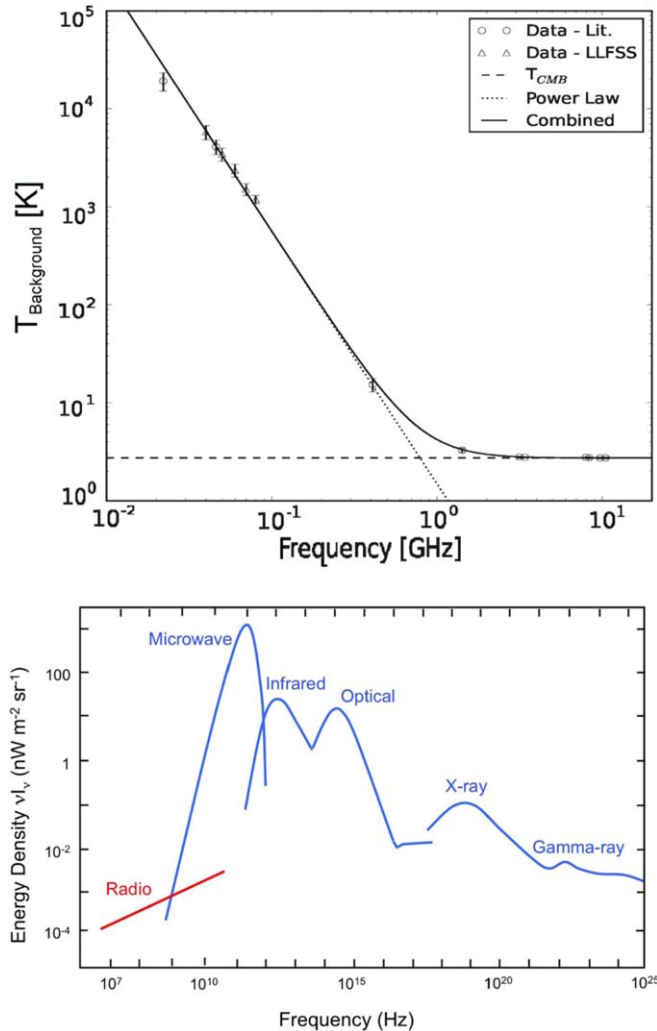


Figure 1. Top: the radio sky zero level in radiometric temperature units, reproduced from Dowell & Taylor (2018), as measured by several different instruments or surveys reporting an absolute zero-level calibration. The spectrum has a power law at frequencies below ~ 10 GHz above the CMB level. Results are shown for ARCADE 2 at 3–10 GHz (Fixsen et al. 2011), Reich & Reich (1986) at 1.4 GHz, Haslam et al. (1982) at 408 MHz, Maeda et al. (1999) at 45 MHz, and Roger et al. (1999) at 22 MHz, as well as several points reported by Dowell & Taylor (2018). Bottom: the photon backgrounds in the universe in units of spectral energy surface brightness density. Reproduced from Singal et al. (2018).

and it was conducted in person at the Hotel Barolo in Barolo, Piedmont, Italy. Individuals who participated in the workshop are listed in Table 1. Most participants arrived at Barolo on Tuesday, 2022 June 14 and departed on Saturday, 2022 June 18. The program consisted of presentation and discussion sessions, with the latter featuring both small-group brainstorming and large-group time. The workshop website²⁹ contains a repository of the program and many of the presentation slides.

²⁹ <https://agenda.infn.it/event/28184/>

Table 1
Participants

Name	Institution
Gianni Bernardi	INAF-Istituto di Radioastronomia and Rhodes University
David Bordenave	National Radio Astronomy Observatory and University of Virginia
Enzo Branchini	University of Roma Tre and University of Genoa
Nico Cappelluti	University of Miami
Andrea Caputo	Tel Aviv University and Weizmann Institute of Science and CERN
Isabella P. Carucci	University of Torino and INFN
Jens Chluba	University of Manchester
Alessandro Cuocco	University of Torino and INFN
Chris DiLullo	NASA Goddard Space Flight Center
Anastasia Fialkov	University of Cambridge
Nicolao Fornengo	University of Torino and INFN
Catherine Hale	University of Edinburgh
Stuart Harper	University of Manchester
Sean Heston	Virginia Tech
Gil Holder	University of Illinois at Urbana-Champaign
Alan Kogut	NASA Goddard Space Flight Center
Martin Krause	University of Hertfordshire
Patrick Leahy	University of Manchester
Shikhar Mittal	Tata Institute of Fundamental Research
Raul Monsalve	UC Berkeley and Arizona State Univ. and Universidad Católica
Elena Pinetti	Fermilab and Kavli Institute of Chicago
Sarah Recchia	University of Torino and INFN
Marco Regis	University of Torino and INFN
Jack Singal	University of Richmond
Marco Taoso	University of Torino and INFN
Elisa Todarello	University of Torino and INFN

3. Scientific Overview

An apparent bright high Galactic latitude diffuse radio zero level has been reported since the early era of radio astronomy (Westerhout & Oort 1951; Wyatt 1953), into the 1960s (Costain 1960; Bridle 1967) and has been seen in data from the 1980s (Phillipps et al. 1981; Beuermann et al. 1985). Early analyses simply assumed that the observed intensity was some mixture of an extragalactic background from radio point sources, with the remainder allocated to a Galactic contribution, and neither of these was particularly well constrained at the time. Renewed interest came with combining the ARCADE 2 balloon-based absolute spectrum data from 3 to 90 GHz (Fixsen et al. 2011; Singal et al. 2011) with absolutely calibrated zero-level single-dish degree-scale-resolution radio surveys at lower frequencies (e.g., Haslam et al. 1982), which agreed on a bright radio synchrotron zero level. In part as a result of the first RSB workshop, the Long Wavelength Array (LWA1) collaboration calculated an absolute zero-level calibration and measurement of the sky zero level at 40–80 MHz, which agreed with the level established by ARCADE 2 and the single-dish radio surveys (Dowell & Taylor 2018).

Another relevant recent result is the absolute calibration computed for the Guzmán et al. (2011) 45 MHz and the Landecker & Wielebinski (1970) 150 MHz all-sky maps, and soon to be computed for the Kriele et al. (2022) 159 MHz map, by the EDGES collaboration using measurements from several single-dipole-antenna instruments as discussed in Section 4.18 and Monsalve et al. (2021).

The radio synchrotron zero level as reported by ARCADE 2 and lower-frequency surveys is spatially uniform enough to be considered a “background,” thus it would join the astrophysical backgrounds known in all other regions of the electromagnetic spectrum.

If it is indeed at the level given by Equation (1), which seems to be overwhelmingly likely, the origin of the radio background would be one of the mysteries of contemporary astrophysics. It is difficult to produce the observed level of surface brightness by known processes without violating existing constraints. A brief review of some recent literature on the subject follows.

Some authors (e.g., Subrahmanyan & Cowsik 2013) have proposed that the background originates from a radio halo surrounding the Milky Way. There are important difficulties with a Galactic origin, however. With magnetic field magnitudes of $\sim 1 \mu\text{G}$ determined by radio source rotation measures to be present in the Galactic halo, the same electrons energetic enough to produce the radio synchrotron background at the observed level would also overproduce the observed X-ray background through inverse-Compton emission (Singal et al. 2010). Also, the observed correlation between radio emission and that of the singly ionized carbon line (C II) would imply an overproduction of the observed level of emission from that line above observed levels (Kogut et al. 2011a). Furthermore, independent detailed modeling of the structure of the diffuse radio emission at different frequencies does not support such a large halo (Fornengo et al. 2014). A halo of the necessary size and emissivity would make our Galaxy anomalous among nearby similar spiral galaxies (Singal et al. 2015). Lastly, analyses of the observed polarization of the synchrotron sky seem to disfavor a Galactic origin, as discussed in Section 4.16 of this report.

However an extragalactic origin for the RSB also presents many challenges. Several authors have considered deep radio source counts (Vernstrom et al. 2011, 2014; Condon et al. 2012; Hardcastle et al. 2021) and concluded that if the RSB surface brightness is produced by discrete extragalactic sources they must be a therefore undetected population that is very low flux and therefore very numerous in number, at least an order of magnitude more numerous than the total number of galaxies in the observable universe. These results are in agreement with others who have probed whether active galactic nuclei (AGNs —Draper et al. 2011) or other objects (Singal et al. 2010) are numerous enough and are further discussed in Section 4.4 of this paper.

Works in the literature have noted that if the RSB were produced by sources that follow the known correlation between radio and far-infrared emission in galaxies, the far-infrared background would be overproduced above observed levels (Ponente et al. 2011; Ysard & Lagache 2012), while others have claimed that the correlation may evolve with redshift and have noted the implications for the radio background (Iverson et al. 2010a, 2010b; Magnelli et al. 2015). Other works have investigated the anisotropy power of the RSB, which seems to be too low at gigahertz frequencies (Holder 2014) to trace the distribution of large-scale structure in the universe while being orders of magnitude higher on the same angular scales at megahertz frequencies (Offringa et al. 2022). Observations have ruled out a large signal from the cosmic filamentary structure (Vernstrom et al. 2017). Other important constraints come from considering that the presence of a significant radio background at the redshifts of reionization could have a dramatic effect on the observed HI 21 cm absorption trough as discussed in Feng & Holder (2018), Ewall-Wice et al. (2018), Mirocha & Furlanetto (2018), Fialkov & Barkana (2019), Mondal et al. (2020), Natwariya (2021), Mirabel & Rodriguez (2022), and here in Section 4.19.

Such constraints have led various authors to investigate potential origins such as supernovae of massive population III stars (Biermann et al. 2014), emission from Alfvén reacceleration in merging galaxy clusters (Fang & Linden 2016), an enhancement in the Local Bubble (Sun et al. 2008, although see Section 4.15 of this report), annihilating dark matter (DM) in halos or filaments (Fornengo et al. 2011; Hooper et al. 2012; Fang & Linden 2015; Fortes et al. 2019) or ultracompact halos (Yang et al. 2013), “dark” stars in the early universe (Spolyar et al. 2009), dense nuggets of quarks (Lawson & Zhitnitsky 2013), injections from other potential particle processes as discussed in Cline & Vincent (2014) and Pospelov et al. (2018) and here in Sections 4.10 and 4.20, and accretion onto primordial black holes (PBHs) as discussed here in Sections 4.13 and 4.14.

4. Summary of Individual Presentations

4.1. Introduction and New Measurements—Jack Singal

This talk presented a brief summary of the points of Section 3 and then introduced two new measurements of relevance to the RSB. These are the 310 MHz absolute map to be made with the Green Bank Telescope and custom instrumentation, and the anisotropy power spectrum measurement at 140 MHz made with LOw Frequency ARray (LOFAR—van Haarlem et al. 2013) observations. The former is in preparation while the latter has been completed.

These projects attest to the importance and impact of workshops such as the one that is the subject of this report. The 310 MHz absolute map project was conceived and prioritized at the previous RSB workshop summarized in Singal et al. (2018),

and the anisotropy measurement at 140 MHz with LOFAR was conceived at a previous BAM meeting in 2018.

4.1.1. 310 MHz Absolute Map

The 310 MHz absolute map will be made by utilizing the unique features of the Green Bank telescope (GBT) along with custom instrumentation to enable an accurate absolutely calibrated zero level. The GBT is the world’s largest clear-aperture telescope, allowing an observation of the radio sky without reflections and emissions off of supporting structures; is fully steerable to all azimuthal angles, allowing for the entire visible sky to be mapped and for scans that repeatedly pass through the north celestial pole (NCP); and is located in the National Radio Quiet Zone allowing for minimal radio frequency interference (RFI). The custom instrumentation includes a unique, high edge-taper antenna feed, which will be mounted at the prime focus of the GBT and will underilluminate the GBT dish, and a newly designed balanced correlation receiver, both visualized in Figure 2 and discussed in detail in Section 4.2.

Maps of the diffuse radio emission are of the utmost importance in astronomy and astrophysics, including for CMB and 21 cm cosmology studies, as evidenced by the 408 MHz Haslam et al. (1982) map having over 1000 citations. However, it is the case that these maps did not have an absolute zero-level calibration as a primary goal, and such a calibration is typically derived, as is the case for the Haslam et al. (1982) map, from blocked-aperture observations with limited overlaps with previous, decades-old measurements made with low-resolution dipole antennas such as that of Pauliny-Toth & Shakeshaft (1962). Dipoles have a beam pattern, and blocked apertures have reflections and emissions, which couple an uncertain amount of radiation from the bright Galactic plane, the ground, and other sources into measurements. These absolute calibrations may also have depended on observations of standard flux calibrator sources and instrument gain modeling, which require extrapolations over orders of magnitude in instrument response and the level of the RSB as an unknown offset to flux calibrators. Table 2 lists all radio frequency maps reporting an absolute zero-level calibration available in the literature from the past 40 yr and how they determined their absolute zero level. It can be seen that all current knowledge of the actual level of diffuse astrophysical emission below 2 GHz ultimately derives from dipole-based and/or over 50 yr old low-resolution measurements.

It can therefore be said that no large-area mapping of the diffuse radio emission at megahertz frequencies with an absolute zero-level calibration as a primary goal has ever been made. Therefore, the new 310 MHz map, which will also include full Stokes-parameter polarization information, will provide an essential resource for understanding and constraining almost all Galactic and extragalactic phenomena that



Figure 2. Some photos of the relevant instrumentation for the 310 MHz absolute map project. The top photo shows the custom high edge-taper feed, which will be mounted at the prime focus of the GBT, while the bottom photo shows the custom balanced correlation receiver mounted in a spare GBT prime focus receiver box. The 310 MHz map will have an absolutely calibrated zero-level and polarization information, which will be valuable for CMB, 21 cm, and other studies as discussed in Section 4.1.1.

manifest in, or depend on the understanding of, diffuse radio emission, in addition to definitively measuring the absolute level of the RSB at megahertz frequencies.

The project is scheduled to have an initial, overnight observing run on the GBT in fall 2022, which will result in a porous, part-sky map. The full map will require one night of observing in roughly every other calendar month, will require mounting and demounting of the custom hardware, and will progress subject to the availability of funds.

4.1.2. 140 MHz Anisotropy Measurement

In a recent work (Offringa et al. 2022) we presented the first targeted measurement of the anisotropy power spectrum of the

RSB. We did this measurement at 140 MHz where it is the overwhelmingly dominant photon background. We determined the anisotropy power spectrum on scales ranging from 2° to $0'.2$ with LOFAR observations of two 18 deg^2 fields—one centered on the northern hemisphere coldest patch of radio sky where the Galactic contribution is smallest and one offset from that location by 15° . We found that the anisotropy power is higher than that attributable to the distribution of point sources above $100 \mu\text{Jy}$ in flux. This level of radio anisotropy power indicates that if it results from point sources, those sources are likely at low fluxes and incredibly numerous and likely clustered in a specific manner. This measurement and its implications are discussed in detail in Section 4.3.

4.2. A 310 MHz Absolute Map—David Bordenave

In order to make a new, modern absolutely calibrated zero-level map of the diffuse radio emission as discussed in Section 4.1.1, we are employing several essential strategies. These are:

1. Utilizing the GBT, which has a clear aperture, and thus is not subject to unknown emissions and reflections related to structures in the light path and is fully steerable, allowing scans at constant azimuth to pass through the north celestial pole (NCP) every ~ 15 minutes to provide an unchanging reference point on the sky to verify the gains and receiver noise temperatures.
2. A custom, high edge-taper feed, which underilluminates the GBT dish, greatly reducing spillover pickup from the ground and any other structures beyond the edge of the dish.
3. A custom balanced correlation receiver, which will allow the gain scale to be calibrated absolutely and the receiver noise temperature to be known and near zero.

A photograph of the custom feed is shown in the top panel of Figure 2. It is constructed out of a frame and wire mesh to reduce weight and wind loading and assembles in six segments. The feed was developed with extensive modeling in CST and GRASP8, and its beam pattern has been measured on the GBO test range. Its response is $\sim 15 \text{ dB}$ at 39° off axis, which corresponds to the edge of the GBT dish, thus greatly reducing spillover emission pickup from the ground to around $\sim 11 \text{ K}$. The residual spillover pickup can be estimated with tip scans of the GBT, resulting in a spillover uncertainty of just $\sim 2 \text{ K}$.

A photograph of the receiver as constructed is shown in the bottom panel of Figure 2. The housing seen on the right end contains the front-end amplifier and calibration boards, and the black-paneled housing seen in the middle contains the digitization and control components. These are seen mounted in a spare GBT prime focus receiver box, which will be installed on the GBT in place of the existing prime focus

Table 2
All Relatively Recent Radio Maps Reporting an Absolute Zero-level Calibration

Frequency (MHz)	Map	Instrument	Source of Absolute Zero-level Calibration
22	Roger et al. (1999)	Dipoles above reflecting screen	Scaling relative to 408 MHz Haslam et al. (1982) map at Zenith applied to other elevations
45	Maeda et al. (1999)	Phased array Yagi dipoles	Overlap with Alvarez et al. (1999), itself based on small region overlap with unspecified pedigree
40, 50, 60, 70, 80	Dowell & Taylor (2018)	240 dipole array with synthesized beam	Flux calibrator sources and instrument gain modeling
408	Haslam et al. (1982)	Jodrell Bank 75 m clear-aperture dish	Overlap with blocked-aperture, 7.5 resolution dipole measurement of Pauliny-Toth & Shakeshaft (1962)
1420	Reich & Reich (1986)	Stockert 25 m blocked-aperture dish	Small overlap with wide beam horn-based measurement of Howell & Shakeshaft (1966)
2300	Tello et al. (2013)	blocked-aperture dish	Total-power radiometer calibrated with observations of moon
2326	Jonas et al. (1998)	HartRAO 26 m blocked-aperture dish	Small overlap with horn-based south celestial pole measurement of Bersanelli et al. (1994)

receiver box, while the custom feed will be attached to the front end of the receiver box.

In order to achieve an accurate and precise absolute zero-level calibration, the receiver has a novel balanced correlation design to ensure gain stability and a known and low receiver noise temperature. A receiver design often used for gain stability is the so-called pseudocorrelation receiver, where the output power of a dipole is divided into two isolated receiver chains after being referenced to ground with a balun. Noise in the amplifiers and filters is uncorrelated between the resulting two channels but the sky power is correlated, allowing the statistical elimination of these noise fluctuations in a recombined signal (e.g., Wollack 1995). However, in such a design, any ohmic losses in the transmission line from the feed, balun, and common regions of the power divider are correlated and therefore add a noise temperature to the sky power measurement, the uncertainty of which is then a source of uncertainty in the absolute zero level. In our balanced correlation receiver, rather than splitting the signal after the balun, the voltage signal on each arm of a given dipole is separately referenced to a common ground with its own transmission line and coaxial transition to eliminate this source of correlated noise. A block diagram of the design is shown in the top panel of Figure 3.

There is one independent receiver chain as visualized in the top panel of Figure 3 for each polarization—thus, there are four chains of amplifier, bandpass filter, and analog-to-digital conversion. On the front-end amplifier boards, all channels can be switched to either their antenna arm or a 50 Ω resistive termination, providing a source of calibrated, uncorrelated noise to each channel. In addition, common high- and low-level calibration noise sources are split and injected into all channels to produce correlated noise suitable for hot/cold Y-factor

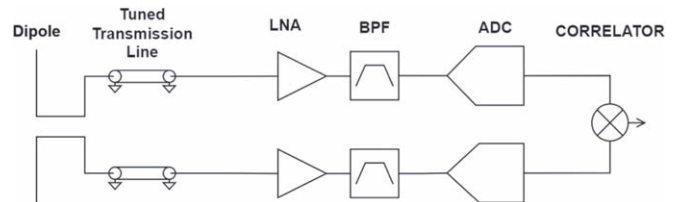


Figure 3. Diagram of the balanced correlation receiver design. “LNA” is low-noise amplifier, “BPF” is bandpass filter, and “ADC” is analog-to-digital conversion. There is one independent receiver chain as visualized here for each polarization.

measurements of the receiver noise. Analog-to-digital conversion takes place in a pair of Ettus Research B210 software-defined radio (SDR) modules, each processing the pair of channels associated with a given dipole. Within the SDRs, the signals are divided into in-phase (“I”) and 90° out of phase (“Q”) components, mixed down, and digitized. These signals are then fast Fourier transformed (FFTs) and correlated in back-end software to give the measured autocorrelated power for each channel and cross-correlated power for all six pairs of channels in spectral bands of ~ 1 MHz in real time and ~ 100 kHz upon further processing over the 20 MHz band. Residual RFI can be filtered further with kurtosis of the spectral signal given these narrow bands.

This will allow the absolute zero-level calibration to be achieved and maintained as follows: (i) Each channel will have its gain measured by recording its output autocorrelation power when its input is terminated in physical loads at 77 K and room temperature. (ii) A measurement of the autocorrelation power when viewing the high and low internal calibration loads and

application of the measured channel gain determines the true precise effective emission temperature of these loads for the channel. (iii) According to basic receiver theory, the gain for the cross-correlation of two channels is the geometric mean of the gains of the two channels. (iv) The receiver noise temperature should be zero or very close to it for the cross-correlations because all noise for any two channels is uncorrelated in the balanced correlation design, and this can be verified by measuring the output cross-correlation power for terminating in the physical loads. (v) With the gain and receiver noise temperature known for all cross-correlations, all Stokes parameters can be determined, with the absolute intensity I being the sum of the two cross-correlations across channels of the same polarization, and the parameters describing the polarization, Q , U , V , being sums and differences of the four cross-correlations across channels of opposite polarization:

$$\begin{aligned} I &= X_1 X_2^* + Y_1 Y_2^* \\ Q &= X_1 X_2^* - Y_1 Y_2^* \\ U &= X_1 Y_2^* - Y_1 X_2^* \\ V &= i(-X_1 Y_2^* - Y_1 X_2^*), \end{aligned} \quad (2)$$

where X and Y represent the two linear polarizations. (vi) The cross-correlation gains and receiver noise temperatures (which should be zero) can be constantly verified in situ during observing by switching in the internal noise sources and because the whole system will view the unchanging NCP every 15 minutes.

The performance of the balanced correlation receiver has been extensively modeled down to the individual circuit element level in Keysight ADS with the model parameters determined with extensive vector network analyzer measurements of the S parameters of the elements. The receiver noise temperatures and their uncertainties are low enough that the total uncertainty in the absolute zero level due to the receiver is ~ 4 K, which adds in quadrature to that due to spillover pickup for a total zero-level uncertainty of 5 K, much less than the sky temperatures at 310 MHz.

4.3. Anisotropy of the RSB at 140 MHz—Sean Heston

As mentioned in Section 4.1.2, we performed the first targeted measurement of the power spectrum of anisotropies of the RSB at megahertz frequencies, where it is the dominant photon background (see the top panel of Figure 1). This area of RSB research is relatively unexplored. Previous studies of temperature power spectra for different frequencies have helped to confirm the source populations for the cosmic infrared (e.g., Ade et al. 2011; George et al. 2015) and gamma-ray (e.g., Broderick et al. 2014) backgrounds and have been a critically important part of CMB science so far (e.g., Aghanim et al. 2020b).

We measured the anisotropy power spectrum of the RSB with two observation fields, each 18 deg^2 , taken by LOFAR at 140 MHz. Our primary field (Field A) was centered on the Galactic northern hemisphere “coldest patch” (Kogut et al. 2011a): $9^{\text{h}} 38^{\text{m}} 41^{\text{s}} +30^{\circ}49'12''$, $l = 196^{\circ}0$ $b = 48^{\circ}0$, which is the area of lowest measured diffuse emission absolute temperature and thus where the integrated line-of-sight contribution through the Galactic component is minimal. LOFAR allows for a simultaneous observation of a separate field offset by 15° in an adjacent 48 MHz wide band, so we selected a location closer to the northern Galactic Pole from the coldest patch (Field B) $10^{\text{h}} 25^{\text{m}} 00^{\text{s}} +30^{\circ}00'00''$ ($l = 199^{\circ}0$ $b = 57^{\circ}9$). Field B should have more, but nearly minimal, total Galactic contribution when compared to Field A.

We performed direction-independent calibration on the two measurement fields, using a manual calibration approach for the coldest patch field (Field A) and an automated calibration for the offset field (Field B). The manual and automated calibrations have similar results, which is why Field B was calibrated using the automated approach. We then extracted the angular power spectra of the fields using the calibrated images. The details of the calibration and power spectra extraction processes are outlined in Offringa et al. (2022).

The results for the power spectra extraction process are shown as the thick purple (Field A) and cyan (Field B) lines in Figure 4. Also shown are twelve 4 MHz wide subbands of Field A (thin lines). The separation of these subbands comes from the spectral dependence of synchrotron radiation, causing the lowest frequency band to have ~ 17 times more power than the highest frequency subband. The full bandwidth (Field A) has a lower angular power due to a more complete $u-v$ coverage. The red square is the $30''$ scaled rms noise of Field A calculated by the procedure described in Holder (2014), which agrees at the relevant angular scale. Older gigahertz-scale measurements are also shown as triangles, diamonds, and a pentagon, again calculated using Holder (2014). Finally, we show the estimated contribution from system noise as the dashed line. We see that our measured power is much higher than what is suggested by the previous gigahertz-scale measurements. Our measurements are also not dominated by system noise, as seen by the large spacing between the measured field lines and the dashed noise line.

Field B’s angular power is larger by a factor of ~ 1.4 in the $(\Delta T)^2$ normalization (therefore ~ 1.2 for ΔT) than the angular power field A. This factor is also the square of the ratio of the average absolute brightness of the two fields in radiometric temperature (Kelvin) units calculated from the map of Haslam et al. (1982). The differences in observed absolute brightness between the fields should only come from differences in lines of sight through the Galactic diffuse component. This is a strong indication that the proportion of angular power, in (Δt) units, due to Galactic structure, traces the proportion of absolute brightness due to that structure for lines of sight with

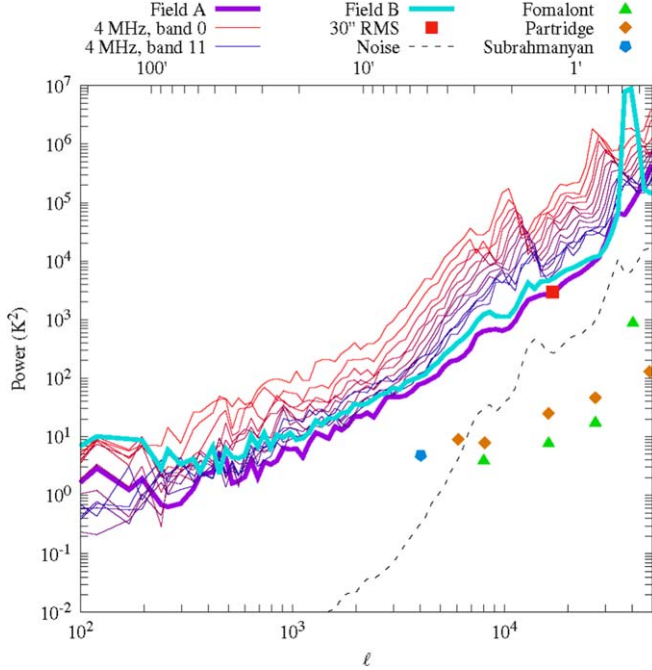


Figure 4. Measured anisotropy power spectrum of the radio sky centered at 140 MHz with an rms noise of $720 \mu\text{Jy}$. Shown are curves for the full bandwidth of the coldest patch field (field A) and the secondary field (field B), as well as for twelve 4 MHz wide subbands of field A. The anisotropy in field A deduced by considering the average noise per beam in the image with the synthesized beam tapered to $30''$ FWHM is also shown and agrees at the relevant angular scale. We also show comparison levels inferred by the noise per beam at 8.7, 8.4, and 4.9 GHz in different fields as calculated by Holder (2014) and scaled here to 140 MHz assuming a synchrotron power law of -2.6 in radiometric temperature units. The amount of angular power is ~ 1.4 times higher for field B compared to field A (in K^2 units) across a range of angular scales. All angular powers are expressed here in the $(\Delta T)_\ell^2$ normalization. Reproduced from Offringa et al. (2022).

minimal Galactic structure and probably for lines of sight far away from the Galactic plane. We believe that this suggests that the contribution from Galactic is subdominant as the normalized angular power $\left(\frac{\Delta T}{T}\right)$ is the same for both fields and the Galactic structure is what varies spatially between our two fields.

In order to account for possibly unremoved point sources below detection threshold in our observation fields, we created a Monte Carlo catalog of simulated sources from $100 \mu\text{Jy}$ to 40 mJy following the flux distribution of Franzen et al. (2016). We placed these sources both randomly in R.A. and decl. as well as using simple sinusoidal clustering on scales of $1'$ and $10'$. We then imaged the point-source files and ran them through the power spectrum pipeline. The results for this analysis are shown in Figure 5 of Offringa et al. (2022). We found that the measured anisotropy power cannot be attributed to potentially unremoved point sources that follow the Franzen flux distribution.

We then decided to test much dimmer and more numerous point sources, specifically a model from Condon et al. (2012) with the least number of sources, which is meant to reproduce the measured radio surface brightness of the sky. We again modeled these point-source distributions with random positions as well as sinusoidally clustered, but only on scales of $1'$. The resulting power spectra of these source populations are also shown in Figure 5 of Offringa et al. (2022). We found that neither model, with and without clustering, produced enough angular power. However, we saw that the clustered model had increased angular power on all angular scales smaller than the clustering scale. Therefore, we are investigating whether a model of very faint but extremely numerous point sources, with the right clustering on multiple angular scales, can reproduce the measured anisotropy power.

4.4. Source Populations in the Extragalactic Radio Sky— Catherine Hale

Our knowledge of the total radio background level that is specifically contributed by known extragalactic source classes is being transformed by recent surveys, which are allowing us to push deeper to understand whether the contribution of faint radio sources can be reconciled with measurements of the sky background level as discussed in Section 3. Works such as Vernstrom et al. (2014), Murphy & Chary (2018), Hardcastle et al. (2021), Matthews et al. (2021), and Hale et al. (2021) have all studied contributions of extragalactic radio sources to the excess sky background temperature (between 144 MHz and 3 GHz) but all find total temperature contributions from extragalactic sources a factor of ~ 4 smaller than the RSB level discussed in Section 1. Below the nominal 5σ detection limit, extrapolations of the source counts using stacking (see, e.g., Zwart et al. 2015) and $P(D)$ analysis (see, e.g., Vernstrom et al. 2014; Matthews et al. 2021) from extragalactic radio images are unable to detect an extremely numerous faint population of sources that would reconcile with the measured RSB level. Recent work by Matthews et al. (2021) has considered the contribution of both AGNs and star-forming galaxies (SFGs) to the extragalactic sky background temperature combining $P(D)$ analysis for the source counts and using evolving local luminosity functions at $z=0$ for AGNs and SFGs. They find a limiting total background temperature contribution of $\sim 110 \text{ mK}$ at 1.4 GHz even down to 10 nJy . This work therefore suggests that the known extragalactic contributions from AGNs and SFGs cannot account for the measured level of the RSB.

As we move to the future of radio surveys, directly detecting faint radio populations (and being able to probe below 5σ) will rely on surveys from telescopes such as the Australian Square Kilometre Array Pathfinder (ASKAP—Johnston et al. 2007; Hotan et al. 2014, 2021), the Meer Karoo Array Telescope (MeerKAT—Booth et al. 2009; Jonas 2009; Jonas 2016),

LOFAR (van Haarlem et al. 2013), and eventually the next-generation Very Large Array (ngVLA—Murphy et al. 2018) and the Square Kilometre Array Observatory (SKAO—e.g., Wilman et al. 2008). These facilities will all push observations to unprecedented sensitivities. However, with this increased depth also comes challenges of source confusion, which is only possible to be overcome by high angular resolution. Recently, at low frequencies (<200 MHz), LOFAR has demonstrated that they are able to overcome such resolution issues, making use of their array stations spread across Europe (see, e.g., Morabito et al. 2022; Sweijen et al. 2022). At higher frequencies (~ 1 GHz), subarcsecond imaging has been observed using telescopes such as e-MERLIN (e.g., Muxlow et al. 2018) and the Very Long Baseline Array (VLBA; see, e.g., Herrera Ruiz et al. 2017) and at higher frequencies still, subarcsecond resolution is already possible with surveys such as the VLA for frequencies at the *S* band and above (see, e.g., Smolčić et al. 2017). However, the combination of depth, sensitivity, and resolution that allows us to determine the contribution of faint sources to the extragalactic radio background and minimize the effects of cosmic variance will rely on LOFAR, ngVLA, and SKAO observations. With these we will be able to probe to sub- μ Jy depths and consider whether an even fainter population of extragalactic sources can account for the level of the RSB.

4.5. The LWA1 Sky Survey—Chris DiLullo

Low-frequency measurements of the sky below 200 MHz are important for determining the nature of the radio synchrotron background. Combined with higher-frequency observations, they can determine the spectral index of the background and help constrain if there is evidence of a spectral break in the power law. They are also important for modern 21 cm cosmology experiments aiming to detect the redshifted 21 cm signal from neutral hydrogen present during Cosmic Dawn and the Epoch of Reionization as they map the Galactic foregrounds, which have to be removed to detect the cosmological signal.

The LWA1 Low Frequency Sky Survey (LLFSS; Dowell et al. 2017) offers some of the only zero-level absolutely calibrated maps of the sky below 100 MHz. The first station of the Long Wavelength Array, LWA1, is an array consisting of 256 dipoles within a $100\text{ m} \times 110\text{ m}$ area along with five outrigger antennas (Taylor et al. 2012). It offers three data-collecting modes: Transient Buffer Narrow (TBN), Transient Buffer Wide (TBW), and a beamformer mode. The TBN and TBW modes are raw voltage modes that record the raw voltages from the antennas either continuously for a narrow bandwidth or for a short duration for the entire 80 MHz of bandwidth offered by the array, respectively. The survey was carried out by collecting TBW data between 10 and 88 MHz for a duration of 61 ms every 15 minutes over 2 days. These

data were then correlated and imaged using the LWA Software Library (LSL; Dowell et al. 2012).

The survey’s total power calibration is derived from custom front-end electronics boards which were designed for the Large Aperture Experiment to Detect the Dark Ages (LEDA; Price et al. 2018). These custom radiometers are connected to the outrigger antennas and provide a means to measure antenna temperature via a three-state switching technique that is commonly used in other 21 cm experiments. LEDA data were used to provide a scaling between observed power and temperature for the survey data.

The LLFSS provides absolutely calibrated maps of the sky at nine frequencies ranging from 35 to 80 MHz. These data have been used to estimate the temperature of the extragalactic radio background (Dowell & Taylor 2018). In that work, the authors model and remove the Galactic contribution to the LLFSS data and find that the remaining extragalactic contribution obeys an expected power law and is consistent with the ARCADE 2 results (Fixsen et al. 2011; Singal et al. 2011). A summary of the results can be seen in the top panel of Figure 1. They also note that the extragalactic radio background, when considered with the results of ARCADE 2, shows no sign of a spectral break or turnover. However, they note that the results are highly dependent on how the Galactic foreground is removed and also the underlying calibration of the LLFSS.

Current efforts to improve the LLFSS have focused on directly measuring the impedance mismatch between the LWA antenna and the front-end electronics. The impedance mismatch correction in the current LLFSS is based on simulations (Hicks et al. 2012) and is a key step in setting the flux scale for the entire survey. Therefore, accurate measurements are necessary to improve the calibration of the survey. Preliminary measurements have been made and in situ measurements at the telescope are being planned for the near future. A new survey is also underway, which will offer more data with which to build the sky maps and possibly increased frequency coverage.

4.6. C-BASS: An All-sky Survey of Galactic Emission at 5 GHz in Intensity and Polarization—Stuart Harper

The study of Galactic synchrotron emission in the optically thin regime has been dominated over the last few decades by the full-sky map of the Galaxy at 408 MHz (Haslam et al. 1982). The 408 MHz map has been critical to the success of recent CMB missions (e.g., Aghanim et al. 2020c) and to our understanding of Galactic synchrotron emission produced by cosmic-ray leptons propagating through the Galactic magnetic field (Rybicki & Lightman 1979). However, the 408 MHz is limited to total intensity only. Measurements of the polarized Galactic emission will be required to study features of the Galactic magnetic field and will be necessary for future CMB missions such as Simons Observatory (Ade et al. 2019) and LiteBIRD (Hazumi et al. 2020) to detect the polarized B-mode

emission produced by primordial gravitational waves. To date, there are very few maps of Galactic polarized emission. The 1.4 GHz Dominion Radio Astronomy Observatory (DRAO)/Villa-Elisa all-sky map (Wolleben et al. 2006; Testori et al. 2008) has been shown to have many systematic errors (Weiland et al. 2022), while the 2.3 GHz *S*-band Polarization All Sky Survey (S-PASS) map (Carretti et al. 2019) only covers the southern sky. Also, at frequencies below 5 GHz Faraday rotation—polarization angle rotation of radiation traversing a magneto-ionic plasma—starts becoming a serious issue even at high latitudes. Simple corrections for Faraday rotation using data from extragalactic polarized sources (Hutschenreuter et al. 2022) is nontrivial since the distances to many high-latitude structures are uncertain and likely have multiple Faraday screens along each line of sight.

The C-Band All-Sky Survey (C-BASS) project will produce an all-sky map of Galactic synchrotron emission at 5 GHz with a resolution of 1° FWHM in both total intensity and polarization. The C-BASS project is a collaboration between the University of Manchester and Oxford in the UK, Caltech in the US, and University of Kwazulu-Natal and the South African Radio Astronomy Observatory in South Africa. The project is a combination of a northern survey based in the Owens Valley Radio Observatory, observations were taken between 2012 and 2015, and the final data processing is expected to be finished later in 2022. The southern survey is based in the Karoo national park in South Africa, with observations currently ongoing.

The Northern C-BASS instrument is a cryogenically cooled dual circularly polarized radiometer that can simultaneously measure Stokes I , Q , and U (Jones et al. 2018). The bandpass spans 4.5–5.5 GHz but a notch filter is used to suppress the central 0.5 GHz due to RFI. For the C-BASS South instrument the receiver design will be updated to include a 128 channel spectrometer that will allow for the accurate excision of RFI and the measurement of in-band Faraday rotation.

The C-BASS North telescope is a 6.1 m dish with a Gregorian design while the C-BASS South has a 7.3 m dish and a Cassegrain design. The C-BASS South primary is highly underilluminated in order to match the main beam to that of the northern telescope. The C-BASS optics were designed to ensure a circularly symmetric beam pattern by having the on-axis secondary reflector supported by a low-loss dielectric foam cone instead of support struts. Far sidelobe contamination was minimized by surrounding the primary with a radio-absorbing baffle (Holler et al. 2013).

The top panel of Figure 5 shows the C-BASS North total intensity map, while the bottom panel shows the polarized intensity map with the polarization vectors overlaid using the `Healpy` line-integral convolution routine (Górski et al. 2005). In total intensity the location of known radio loops (Vidal et al. 2015) has been overlaid. The polarized intensity map has a noise level of 0.1–0.2 mK rms per deg^2 , which will allow for

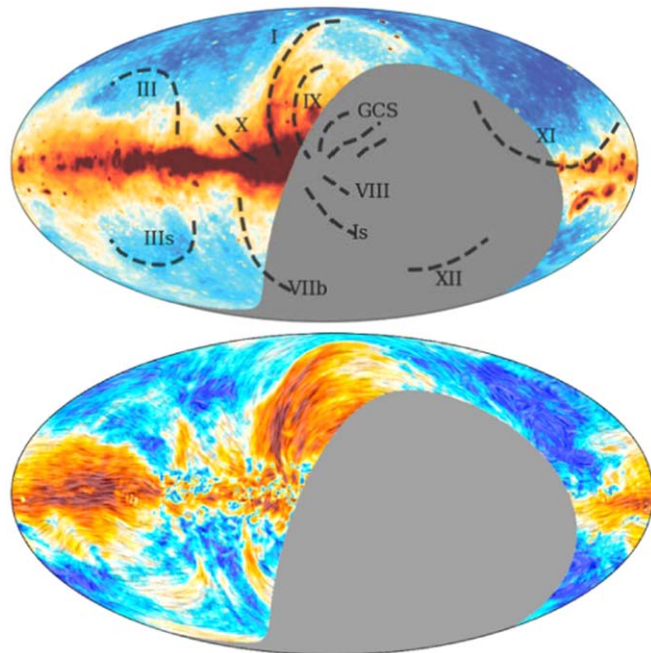


Figure 5. C-BASS North maps of total intensity (top) and polarized intensity (bottom) in Galactic coordinates using a Mollweide projection. The total intensity map color scale has been saturated along the Galactic plane and includes the locations of well-known radio loops (Vidal et al. 2015). The polarized intensity map has the projected B-field direction overlaid using line-integral convolution.

the constraint of polarized synchrotron down to a level of $\sim 0.75 \mu\text{K-arcmin}^2$ at 100 GHz. The signal-to-noise ratio (S/N) of the C-BASS polarization data is greater than 5 for more than 95% of the sky at 1° resolution, with Faraday rotation angles less than 5° for regions away from the Galactic plane—for lower-frequency surveys, like S-PASS, this value is typically a factor of 3–4 times larger.

The final C-BASS map will be the highest S/N and the most robust template of Galactic synchrotron emission for studies of the CMB and Galactic astrophysics for the foreseeable future.

4.7. C-BASS: Polarization in the Northern Hemisphere: Fractional Polarization and Constraints on Field Tangling—Patrick Leahy

Synchrotron polarization is a powerful diagnostic of the structure of the Galactic magnetic field. Its intrinsic polarization is $\approx 75\%$ (for spectral index $\alpha \approx -1$), but, as observed, this is reduced by averaging different field orientations along the line of sight and across the beam, as well as by differential Faraday rotation at long wavelengths. Synchrotron polarization therefore gives two independent measures of the tangling of the field: the observed pattern of the polarization angle χ on the sky, and its fractional polarization, m . Any extragalactic radio background is expected to have negligible polarization unless

observed at a very high resolution that can resolve it into individual sources, since polarization orientation should not be correlated over cosmological distances.

As described in Section 4.6, C-BASS provides our best view of the Galactic polarized emission, with minimal Faraday distortion and far higher S/N than WMAP and Planck. In particular, in those missions, synchrotron cannot be accurately separated from other emission processes, leaving the fractional polarization uncertain by factors of several (e.g., Vidal et al. 2015).

C-BASS does not measure the overall zero level, and so we have set this using the ARCADE 2 maps at 3, 8, and 10 GHz (Fixsen et al. 2011): After subtracting the CMB monopole and dipole, we interpolated to the C-BASS frequency of 4.76 GHz assuming a power-law spectrum in each pixel, and fitted the result directly to the C-BASS map, convolved to ARCADE resolution and also with the CMB dipole subtracted, in the same set of pixels. We estimate about 5 mK uncertainty, limited by residual systematics in ARCADE.

Apart from a narrow region along the Galactic plane where Faraday depolarization is still significant, C-BASS shows a field pattern ordered on scales much larger than our 1° beam (Figure 5). This applies not only in the prominent discrete “loops” and “spurs,” but also in high-latitude regions well away from these structures, where lines of sight presumably sample typical paths through the thick synchrotron-emitting disk. To quantify this, we measured the position angle structure function, $D(\Delta\theta) = \langle (\chi(\hat{n}) - \chi(\hat{m}))^2 \rangle$, where the average is over all pairs of directions \hat{n} and \hat{m} separated by angle $\Delta\theta$. We used parallel transport to ensure this function is coordinate independent, and polarization angle differences are folded into $|\Delta\chi| \leq 90^\circ$. Random polarization angles would give $\sqrt{D/2} = 37^\circ$. The results are plotted in Figure 6. We restricted our analysis to the northern high-latitude sky, $b > 30^\circ$, excluding regions affected by the high-latitude Loops I and III. $\sqrt{D/2}$ flattens off at about $\Delta\theta_0 = 15^\circ$, although there is a residual large-scale order since the value stays significantly below 37° out to beyond $\Delta\theta = 40^\circ$. For a simple model in which the field is coherent over scales d on a path-length L , we expect $N = L/d$ cells on a line of sight, and the structure function will flatten at $\sin(\Delta\theta_0/2) \approx 1/N$; so, our result suggests $N \approx 7.7$. This model gives a random walk in polarization space (Q , U) with N steps, hence reducing the polarization fraction by \sqrt{N} , and so predicts $m = 75\% / \sqrt{7.7} \approx 27\%$. This is highly inconsistent with the observations, which have $\langle m \rangle = 3.3\%$ in the same region, and hardly any pixels with $m > 10\%$. The low observed m in this “empty” region of sky also contrasts with much higher values in discrete features like Loop I (the North Polar Spur), where the raw polarization reaches up to $\approx 30\%$ without any correction for an underlying weakly polarized background.

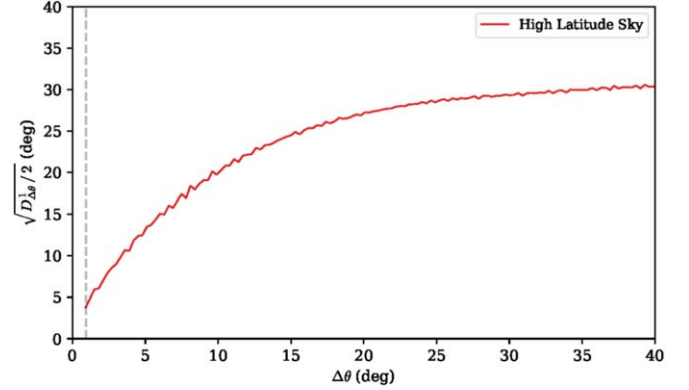


Figure 6. $\sqrt{D/2}$ vs. separation $\Delta\theta$ for the high-latitude C-BASS polarization angles, where D is the structure function, so $\sqrt{D/2}$ would equal the standard deviation, on scales large enough that pixel pairs are uncorrelated.

At first sight, we might invoke an unpolarized isotropic background to resolve the paradox. But this does not work (although see Section 4.16): The ARCADE model of Seiffert et al. (2011) implies a contribution of 16.4 mK at our frequency, which reduces the average Stokes I brightness in our region by less than a factor of 2, rather than the factor of 8 required. Nor are we convinced by the original arguments of Kogut et al. (2011a) for such an extragalactic background: The misfit to a slab model ($\text{csc}|b|$ law) or tracers of the thin disk, such as [C II], is anisotropic, so at least partly local; the minimum synchrotron emission in both hemispheres is at intermediate latitudes, and there are large variations between galactic quadrants even excluding the loops. We see no reason to invoke a separate cosmological excess as well.

A second resolution would invoke multiscale tangling in the magnetic field, so that the large-scale order visible in the polarization angles is superimposed on a much finer-scale tangling unresolved by C-BASS. Such a single-scale model is doubtless oversimplified, but a power-law spectrum of field fluctuations cannot resolve the problem: Only a very steep angular power spectrum can produce the large-scale order observed, and then the small-scale fluctuations are too weak to cause depolarization. Leclercq (2017) measured the angular power spectrum of the diffuse polarized emission on scales down to $3/4$ in the Arecibo G-Alfa Continuum Survey (GALFACTS—Taylor & Salter 2010) and found that $C_l^{E,B}$ mostly declined faster than $\ell^{-2.6}$ in the set of $15^\circ \times 15^\circ$ region considered, which is too steep for the fine-scale fluctuations to cause substantial depolarization.

A third resolution would be a fortuitous cancellation of polarization along the line of sight, for instance if the thick-disk (or halo) field was nearly orthogonal to that in the thin disk.

Since none of these resolutions are particularly satisfactory, the low fractional polarization of the high-latitude synchrotron

emission remains a major puzzle and merits further analysis including more realistic modeling.

4.8. A Cross-correlation Analysis of CMB Lensing and Radio Galaxy Maps—Giulia Piccirilli

Besides the large amplitudes of the RSB discussed in Section 3 and that of the dipole in the spatial distribution of the radio sources (see Peebles 2022 and references therein), there is yet one more anomaly that characterizes the radio sky: the high amplitude of the two-point autocorrelation function of the radio sources in the TGSS-ADR1 catalog (TGSS—Intema et al. 2017) at large angular scales (Dolfi et al. 2019). Whether this is a genuine feature or an artifact due to unidentified systematic errors in the data analysis, it is a question that we have addressed by cross-correlating the angular position of the TGSS sources (since only a small fraction of them have measured redshifts) with the angular map of an unbiased tracer of the underlying mass density field. For the latter, we considered the lensing map of the CMB (Aghanim et al. 2020c). The motivations for studying this cross-correlation are several. First, the two maps are expected to be prone to different systematic errors. Even when they are not properly identified and corrected for, these errors are not supposed to correlate with each other and therefore should not contribute to the cross-correlation statistics. In addition, correlating the angular position of some biased mass tracer of the mass field, like the radio sources, characterized by a redshift-dependent bias $b(z)$ and a redshift distribution $N(z)$, with that of unbiased tracers allows us to break the degeneracy of these two functions. This is clear from the expression of the cross-angular spectrum below:

$$\begin{aligned}
 &= \frac{2}{\pi} \int_0^\infty dz W^g(z) \int_0^\infty dz' W^k(z') \\
 &\quad \times \int_0^\infty dk k^2 P(k; z; z') j_\ell[k\chi(z)] j_\ell[k\chi(z')]. \quad (3)
 \end{aligned}$$

In Equation (3), the window function $W^g(z)$ of the biased tracers depends on the product $b(z) \times N(z)$, whereas the window function of the lensing signal $W^k(z)$ does not. Therefore, combining the cross-spectrum with the autospectrum of the tracers (that is proportional to $[W^g(z)]^2$) and with that of the lensing signal (that depends on $[W^k(z)]^2$) can potentially break this degeneracy. As a result, the cross-correlation analysis is expected to be less biased and, in combination with the autocorrelation, it is able to provide information on clustering properties and on the nature of the radio sources.

From our cross-correlation analysis, we obtained three main results:

1. First of all we detected the TGSS–CMB convergence cross-correlation signal with 12σ significance. As shown in Figure 7, the measured cross-spectrum is in good

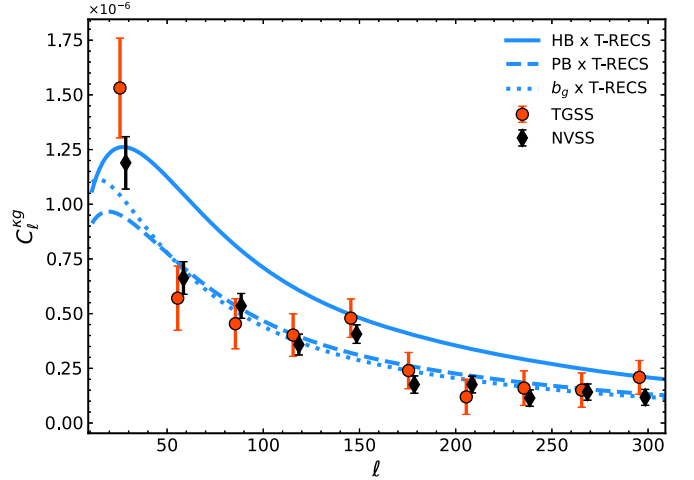


Figure 7. Measured cross-spectrum κ_g of TGSS–CMB lensing (red dots) and NVSS–CMB lensing (black diamonds). Error bars represent the 1σ uncertainties obtained assuming Gaussian statistics. Blue curves represent model predictions obtained using different prescriptions for the bias, $b(z)$, while the T-RECS $N(z)$ distribution of Bonaldi et al. (2018) is used (see Piccirilli et al. 2022 for a detailed description).

agreement with the one obtained using the radio sources of the NVSS catalog (NVSS—Condon et al. 1998), whose autospectrum does not show a similar excess. We then conclude that the power excess originally detected in the TGSS autospectrum on large angular scale probably originates from unidentified systematic observational effects.

2. After having verified the genuine nature of the two cross-correlation signals, we tried to fit the measured cross-spectra with theoretical models for $b(z) \times N(z)$ taken from the literature. To do so, we performed two χ^2 tests: the first one uses the cross-spectrum only, while the second one uses both the cross- and autospectra. For the $b(z)$ model of both TGSS and NVSS sources we considered two cases, both based on the Halo Model (HM—Cooray & Sheth 2002): (i) the Halo Bias (HB) model of Ferramacho et al. (2014), in which different types of radio sources are assigned to halos of different masses and biases; (ii) the Parametric Bias (PB) model proposed by Nusser & Tiwari (2015) to fit the angular spectrum of the NVSS sources.

For both TGSS and NVSS catalogs, we found that models that can fit the large angular scales overpredict the power on smaller scales and are ruled out (e.g., $\chi^2 = 4.88$; the HB model in Figure 7) while the other ones perform similarly well in describing the behavior of the estimated spectra on all scales but the largest ones (e.g., $\chi^2 = 1.59$, PB model in Figure 7). These results are robust against the choice of the $N(z)$ model and to the

potential systematic errors that may affect the radio catalogs.

- As the models proposed in literature to match the NVSS and TGSS autospectra do not provide a good fit to the cross-spectra, we tried to constrain the $b(z)$ model from data keeping the $N(z)$ and cosmological model fixed. We did not leave $N(z)$ free to vary since, as we have seen, our results are quite insensitive to the choice of different redshift distribution model. Following Alonso et al. (2021) and given the limited number of data points in our analysis, we considered two simple bias models that depend upon one single parameter, the effective linear bias b_g . Focusing on the joint analysis of the NVSS catalog, we find that the nonevolving b_g model (shown with a dotted line in Figure 7) fits both the auto- and cross-spectrum on large angular scales better than the one that evolves with the redshift. The reason for this is that the constant bias model gives more statistical weights to the nearby, low-redshift sources that dominate the cross-correlation signal at low multipoles.

Our results indicate that, even after reducing the contribution of spurious signals through the cross-correlation technique, the clustering amplitude of the radio sources on angular scales of 10° remains large with respect to Λ CDM prediction for a population of radio objects with an $N(z)$ consistent with their observed luminosity function and with the expectation of the halo model bias. The excess is not large but is systematically detected in all models explored. The excess can, at least in part, be accounted for by advocating for a large, constant bias factor b_g with magnitude comparable with that of the bright QSOs at high redshift, which, however, is difficult to reconcile with the presence of the mildly biased star-forming galaxies that dominate the population of radio sources at low redshifts. Alternative models of a decreasing bias as a function of redshift proposed by Negrello et al. (2006) did not improve the quality of the fit. Our results therefore hint at a large-scale clustering excess of the radio sources in the 100 MHz–1 GHz band, but are not conclusive with respect to its interpretation. For that we will have to wait for next-generation wide surveys of a much larger number of sources like SKA precursors or, on the shorter term, for complementary analyses in other radio bands like the one that is being carried out by the LOFAR team.

4.9. The Radio SZ Effect—Gil Holder

The Sunyaev–Zel’dovich (SZ) effect (e.g., Sunyaev & Zeldovich 1980) arises due to the inverse-Compton upscattering of photons by energetic electrons, causing a distortion to the base photon spectrum. It was originally, and has commonly been, understood in the context of the CMB, where the hot electrons of galaxy clusters distort the CMB blackbody in a detectable way when viewed in the direction of a cluster, with an increment in the observed surface brightness and

radiometric temperature at higher frequencies and a decrement at lower frequencies. The CMB SZ effect has been a major focus of CMB science and the study of clusters for cosmology and other purposes (e.g., Battistelli et al. 2019).

In Holder & Chluba (2022), we noted that the RSB, if it is extragalactic, would act as an ambient photon field for clusters in the same manner as the CMB, and therefore, one would expect a “radio SZ” effect to distort the power-law spectrum of the RSB. Since the base RSB signal is a continuous power law, an SZ signal for the radio alone would be an increment at all observable frequencies. However, in that work we showed that because the CMB is also an appreciable contributor to the total surface brightness at 100s of MHz, and it has an SZ decrement at these frequencies, the radio SZ effect in combination with the CMB SZ signal would result in a null frequency ν_N between 700 and 800 MHz, below which there would be an increment in the observed surface brightness in the direction of a cluster and above which there would be a decrement, with the amount of increment or decrement larger at frequencies farther from the null.

In Lee et al. (2022), we present further calculations of the relativistic and kinematic corrections to the combined RSB and CMB signals, as well as the potential effects of a dipole anisotropy in the RSB as seen by the cluster. The magnitude of the combined radio SZ effect and the exact frequency of the null each depends to varying degrees on the electron temperature T_e and density N_s (often combined in the Compton y parameter $y = k_B T_e N_s / m_e c^2$), the cluster velocity $\beta_c = \frac{v_c}{c}$ and movement direction $\mu_c = \cos \theta_c$, and the presence or absence of a dipole anisotropy in the RSB.

As shown in Lee et al. (2022), realistic models result in a combined signal null between $\sim 730 < \nu_N < \sim 800$ MHz, and, assuming all of the RSB is present at the redshift of a given cluster, a decrease in the radiometric temperature of on the order of ~ 0.25 mK at 1 GHz and an increase on the order of ~ 1 mK at 500 MHz. If one allows the fraction of the current RSB present at higher redshifts $f(z)$ to vary, these increment and decrement magnitudes depend nonlinearly on that fraction—for example, $f(z) = 0.5$ results in a loss of around three-quarters of the radiometric temperature increase at 500 MHz.

From CMB SZ measurements the locations of thousands of clusters are known, and some clusters have measured or constrained values for y , β_c , and μ_c . Several existing radio interferometric facilities in principle have the sensitivity to measure the level of increment or decrement in emission temperature due to the radio SZ effect. This is discussed in Section 5. A detection of the radio SZ effect would confirm the RSB as extragalactic, and its presence or lack thereof in clusters of higher redshift would constrain $f(z)$ and therefore potentially the redshift(s) of origin of the RSB.

4.10. Low-frequency Absolute Spectrum Distortions— Jens Chluba

Spectral distortions of the CMB have now been recognized as an important probe of the early-universe and particle physics (Chluba et al. 2019, 2021). It has been argued that the long-standing limits on the average energy release obtained with COBE/FIRAS (Mather et al. 1994; Fixsen et al. 1996) could principally be improved by more than a factor of $\simeq 10^3$ using modern technology (Kogut et al. 2011a; André et al. 2014). This could provide a litmus test of Λ CDM and potentially even lead to the discovery of signals due to new physics (Chluba et al. 2021).

When thinking about CMB spectral distortions, we frequently fall into the standard μ plus y -distortion picture (Sunyaev & Zeldovich 1970a, 1970b; Burigana et al. 1991; Hu & Silk 1993). However, not only has it become clear that the thermalization process allows for more rich signals when the distortion is created at the transition between efficient and inefficient Compton scattering around redshift $z \simeq 50,000$ (Chluba & Sunyaev 2012; Khatri & Sunyaev 2012; Chluba 2013), it has also been demonstrated that photon injection distortions created at $z \lesssim 10^5$ generally can no longer be categorized using the simple μ/y picture (Chluba 2015; Bolliet et al. 2021).

One prominent example of a photon injection distortion is the cosmological recombination radiation (Dubrovich 1975; Sunyaev & Chluba 2009; Chluba & Ali-Haïmoud 2016), which can tell us about the exact dynamics of the cosmological recombination process and potentially even allows measuring the cosmic expansion history at high redshift (Hart et al. 2020; Hart & Chluba 2023). At $z \lesssim 10^4$, Compton scattering is no longer efficient and photon injection processes essentially imprint the distortion signal that is only affected by redshifting and free-free absorption at low frequencies. The main motivation for thinking about the general photon injection problem was to try to understand if the distortion signals can mimic a power-law dependence at low frequencies due to the combined action of redshifting and scattering. Indeed, photon injection distortions in the low-frequency tail of the CMB, e.g., due to some decaying or annihilation particle, exhibit a rich phenomenology of spectral signals (Chluba 2015; Bolliet et al. 2021) that could be linked to the high RSB level inferred from ARCADE and other measurements discussed in Section 1, if it is of cosmological origin.

However, it appears that injection of photons at single frequencies may not be sufficient even if occurring in the partially Comptonized regime at $10^4 \lesssim z \lesssim 3 \times 10^5$ (Acharya & Chluba 2023). We therefore considered more general photon injection cases with a power-law soft photon spectrum. In Figure 8, we show a few distortion signals created by a decaying DM particle with varying lifetime and injection energy. This is to motivate that indeed it may be possible to

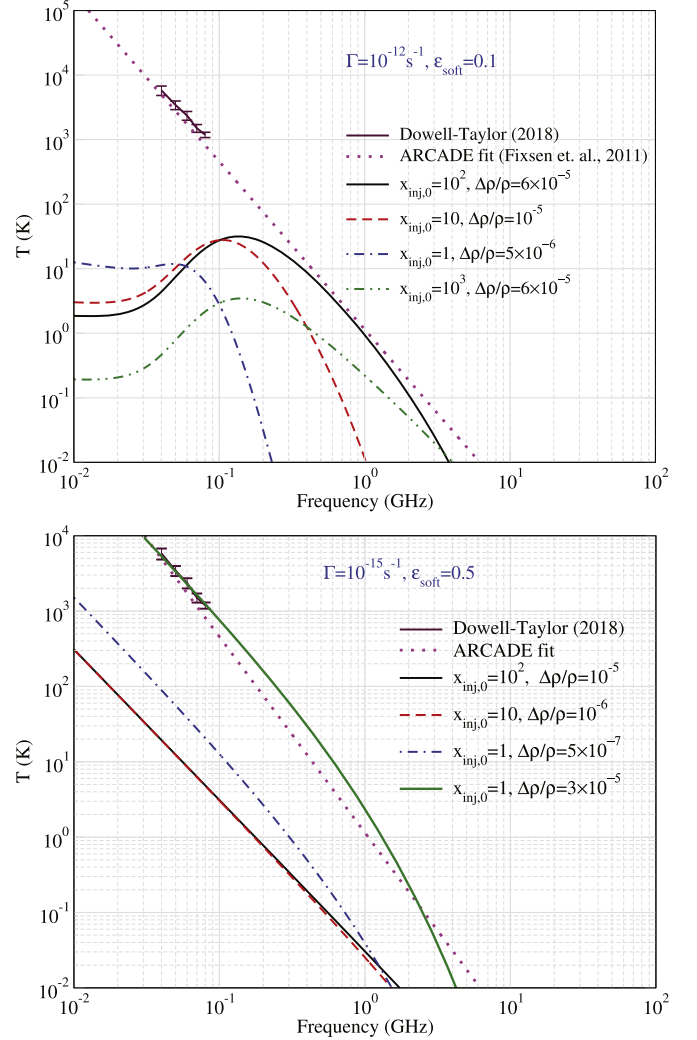


Figure 8. Spectral distortion signals created by free-free-type soft photon injection from a decaying dark matter particle with lifetime $t_x \simeq 10^{12}$ s (top) and 10^{15} s (bottom). In each case, it is assumed that a fraction ϵ_{soft} of the total energy (as labeled) is injected as soft photons. The injection frequency, $x_{\text{inj},0} = h\nu_{\text{inj},0}/kT_0$, is also varied with some of the cases shown coming intriguingly close to the ARCADE RSB level (figures provided by Sandeep Acharya).

create distortions at low frequencies by injecting soft photon spectra (here of free-free type) that come close to reproducing the high RSB level inferred from ARCADE and other measurements. Needless to say, these examples are just for illustration and a more rigorous search for viable solutions is currently in preparation. Overall, it seems clear that new physics examples should consider the interplay with CMB thermalization and scattering physics to open the door to realistic predictions for the source of the RSB level. An early-universe solution for the radio excess would also overcome limitations due to constraints on the fluctuations of the RSB (as discussed in Section 4.3), which other models (e.g., such as the

one presented in Section 4.20) may still suffer from (Acharya & Chluba 2022).

4.11. Constraining Below-threshold Radio Source Counts with Machine Learning—Elisa Todarello

To determine whether there is a new population of faint point sources that give rise to the RSB, we try to develop a new technique to extract low flux density source counts from observational images based on Convolutional Neural Networks (CNN). Below-threshold source counts are usually determined through a statistical analysis of the confusion amplitude distribution, the so-called $P(D)$ method (Scheuer & Statistical Method 1957).

CNNs are well suited for image processing and have proven extremely powerful in pattern recognition. They are also used for counting tasks, such as determining the number of people in a densely packed crowd. It is then interesting to explore whether CNNs are able to outperform the $P(D)$ strategy, or at least to provide a complementary approach.

Our goal is to train a CNN capable of inferring the source count at low flux densities s from interferometric images, such as those of the Evolutionary Map of the Universe radio survey (EMU—Joseph et al. 2019). Specifically, the output we want from the network is the source count in 10 logarithmically spaced flux bins between 10^{-5} and 10^{-7} Jy. Our first task is then to create a suitable training set of simulated images with known source counts. As a starting point, we take the Tiered Radio Extragalactic Continuum Simulation (T-RECS) simulated “medium” catalog of extragalactic sources (Bonaldi et al. 2019) at a frequency of 940 MHz. We truncate the catalog at a minimum flux of 10^{-7} Jy to render the file size manageable. This catalog spans 25 deg^2 and, with our truncation, contains about 30 million sources. The differential number count of sources $n(s) = dN(s)/ds$ reproduces observations. Next, we create new catalogs with a variety of $n(s)$ by modifying the T-RECS catalog. We choose the following functional form with two free parameters α and s_0 :

$$n(s) = \left(1 + \frac{s_0}{s}\right)^\alpha n_{\text{T-RECS}}(s). \quad (4)$$

We consider 21 pairs of α and s_0 as shown in Figure 9. We generate the 21 corresponding catalogs by Monte Carlo sampling $n(s)$. Several of these catalogs contain a number of sources greater than 30 million. We take the properties of the extra sources from the T-RECS “wide” catalog, overwriting their coordinates with random values that fall within our image.

To create the simulated images, we use ASKAPsoft (Yandasoft—Guzman et al. 2019). In the first stage of the simulation, the text catalog is converted into a “sky model,” i.e., an image of the sky without telescope effects. Next, the observation is simulated, the output being the visibilities with instrumental noise added. In the last step, the visibilities are

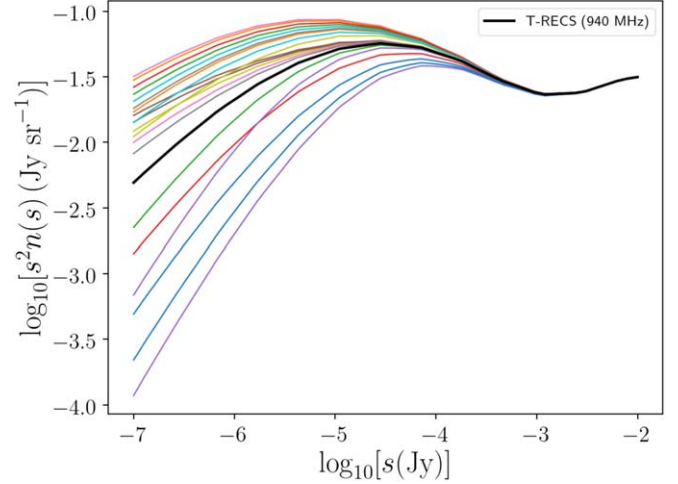


Figure 9. Differential number counts used to create the training set discussed in Section 4.11.

converted to physical space, and deconvolution with the point-spread function is performed with the CLEAN algorithm.

At this point, we have 21 25 deg^2 images, each made of 2560^2 pixels. Since CNNs work more efficiently with low numbers of pixels, we split each image into 400 subimages, for a total of 8400 subimages, most of which we will use as a training set, while the rest will be used for validation and testing. Our CNN comprises three convolutional layers, and one densely connected layer before the output layer with 10 nodes, each corresponding to the source count on one of our bins.

As a first trial, we train the network using the sky model images. The network yields good results after about 500 epochs of training. Figure 10 shows the reconstruction residual in bin i for image j :

$$\Delta N^{ij} = \frac{N_{\text{predicted}}^{ij} - N_{\text{true}}^{ij}}{N_{\text{true}}^{ij}}, \quad (5)$$

where the N^{ij} are obtained by summing over all subimages in the training set that belong to the same 25 deg^2 image.

The worst performance is for images with few sources. However, such low source count are far from expectations. We test that the network is able to reliably reconstruct the number counts for values of α and s_0 it has not seen before. As a stress test, we also create images for which the number count in each bin is assigned at random, within the range of values used for training. In this case, the network does not perform as well, indicating that it has learned the functional shape (Equation (4)) and it is not able to estimate the number of sources in each bin independently from the others. As a solution to this problem, we plan to retrain the CNN with a variety of physically

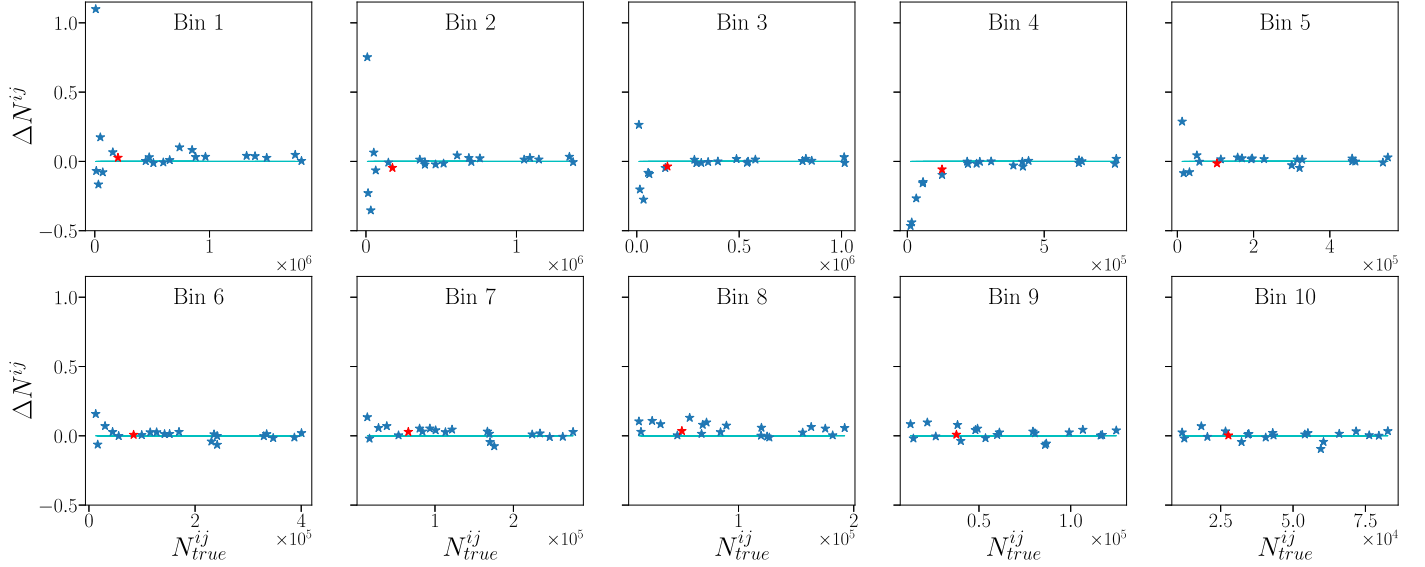


Figure 10. Reconstruction residuals. The red star marks the image having the differential source count $n_{T-RECS}(s)$.

plausible functional shapes, increasing the degrees of freedom from the current two, α and s_0 .

The next and challenging step, which is currently in progress, is to apply the CNN to recover the source count from the restored image that contains noise and confusion.

4.12. Observational Cosmology with the 21 cm Background Radiation (and Radio Background By-products)—Gianni Bernardi

The redshifted 21 cm line promises to be one of the best probes of the formation of early structures during the cosmic dawn and the subsequent epoch of reionization. This has motivated the construction of a new generation of radio instruments that are currently providing increasingly stringent upper limits on the expected signal (Bernardi et al. 2016; Mertens et al. 2020; Trott et al. 2020; Abdurashidova et al. 2022; Barry et al. 2022; Singh et al. 2022), including a “controversial” detection at $z \sim 17$ (Bowman et al. 2018). The challenge that 21 cm observations face is the separation of the cosmological signal from the much brighter foreground emission. The characterization of the foreground spatial and spectral properties has therefore been an active research line over the last decade (e.g., Bernardi et al. 2010, 2013; Dillon et al. 2015; Thyagarajan et al. 2015; Kerrigan et al. 2018; Ghosh et al. 2020; Garsden et al. 2021; Byrne et al. 2022; Cook et al. 2022). Such foreground characterization includes recent observations taken with two different instruments:

1. All-sky maps with the Aperture Array Verification System 2 (AAVS2 Benthem et al. 2021; Macario et al. 2022) as pictured in the top panel of Figure 11. AAVS2 is

a prototype station of the Square Kilometre Array, i.e., a ~ 40 m diameter station equipped with 256 dual-polarization, log-periodic antennas sensitive to sky emission in the 50–350 MHz range. A set of snapshot observations, spanning the whole 0–24^h local sidereal time (LST) range, was carried out in interferometric mode in 2020 April in order to commission the newly deployed system. Each snapshot yielded an all-sky image like the one showed in Figure 11 (middle panel), with angular resolutions between $\sim 1.3^\circ$ and $\sim 8^\circ$. As the telescope was used in drift scan mode, images show the brightness distribution changing as the sky transits overhead.

Despite the limited angular resolution due to the longest baseline being only ~ 40 m, the uv coverage is excellent, with baselines as short as ~ 1 observing wavelength, which corresponds to angular scales as large as hundreds of degrees on the sky. Figure 11 (middle panel) shows an example of how the large-scale emission is accurately imaged in AAVS2 observations: The Galactic plane is visible in its entirety and large-scale and fainter, low-surface brightness features are detected across the whole sky. We found that the calibration accuracy is within 20%, and further analysis can improve it. Future work will be dedicated to include the zero spacing in AAVS2 observations in order to use them to measure the radio spectrum at high Galactic latitudes similarly to Dowell & Taylor (2018).

2. Measurements of the Galactic synchrotron spectrum with LEDA (Bernardi et al. 2015, 2016; Price et al. 2018). LEDA is located at the Owens Valley Radio Observatory and uses four dipoles equipped with custom-built

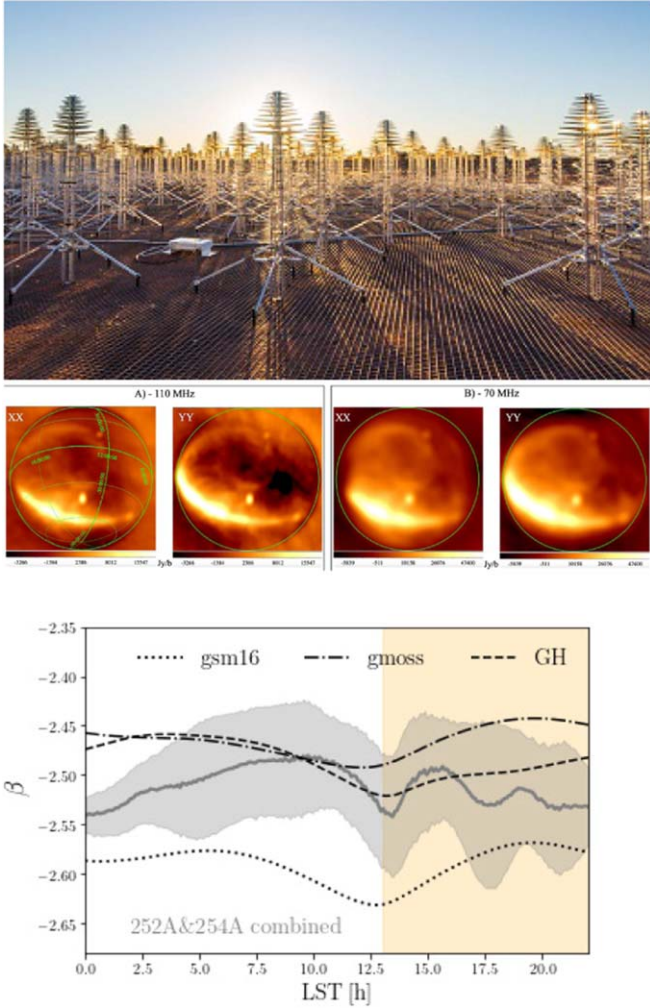


Figure 11. Top: picture of the AAVS2 station with a close-up view of the log-periodic antennas. Adapted from Macario et al. (2022). Middle: examples of all-sky images taken with the AAVS2 station at 110 MHz (panel (A)) and 70 MHz (panel (B)). Both orthogonal polarizations, XX and YY, are displayed. Units are Jy beam^{-1} . Adapted from Macario et al. (2022). Bottom: mean value (gray solid line) and standard deviation (gray area) of the foreground spectral index as a function of LST. Black lines represent prediction extrapolated from other measurements (see Spinelli et al. 2021 for details). The yellow region indicates measurement taken during daytime. Reproduced from Spinelli et al. (2021).

receivers that enable accurate total-power radiometry in the 30–88 MHz range. Absolutely calibrated spectra are obtained every 15 s as a function of LST and two dipoles observed for 137 nights between 2018 and 2019 (Spinelli et al. 2021). Each spectrum T_m is fitted by a power-law model:

$$T_m(\beta, T_{75}) = T_{75} \left(\frac{\nu}{75 \text{ MHz}} \right)^\beta + T_{\text{CMB}}, \quad (6)$$

where β is the synchrotron spectral index, T_{75} is the sky temperature at 75 MHz, ν the observing frequency, and T_{CMB} is the CMB temperature. We found that the spectral index is reasonably constant in the $0^{\text{h}} < \text{LST} < 22^{\text{h}}$ range, varying between -2.48 and -2.54 , with a tight dispersion $\Delta\beta \sim 0.06$ as seen in the bottom panel of Figure 11 (Spinelli et al. 2021). LEDA observations have an accurate absolute calibration and are sensitive to the whole sky emission visible from the Owens Valley Radio Observatory, including the Galactic plane. Future work will be dedicated to model the known (Galactic and extragalactic) contributions to the measured spectrum in order to constrain the contribution of the radio synchrotron background excess.

4.13. Backgrounds from Primordial Black Holes—Nico Cappelluti

In this section, we explore the observational implications of a model in which PBHs with a broad birth mass function ranging in mass from a fraction of a solar mass to $\sim 10^6 M_\odot$, consistent with current observational limits, constitute the DM component in the universe as presented by Cappelluti et al. (2022). The formation and evolution of dark matter and baryonic matter in this PBH- Λ CDM universe are presented.

In this picture, PBH DM mini halos collapse earlier than in standard Λ CDM, baryons cool to form stars at $z \sim 15\text{--}20$, and growing PBHs at these early epochs start to accrete through Bondi capture. The volume emissivity of these sources peaks at $z \sim 20$ and rapidly fades at lower redshifts. As a consequence, PBH DM could also provide a channel to make early black hole seeds and naturally account for the origin of an underlying DM halo/host galaxy and central black hole connection that manifests as the $M_{\text{bh}}\text{--}\sigma$ correlation.

To estimate the luminosity function and contribution to integrated emission power spectrum from these high-redshift PBH DM halos, we develop a Halo Occupation Distribution (HOD) model. In addition to tracing the star formation and reionization history, it permits us to evaluate the cosmic infrared and X-ray backgrounds (CIB and CXB). We find that accretion onto PBHs/AGNs successfully accounts for these detected backgrounds and their cross-correlation, with the inclusion of an additional infrared stellar emission component. Detection of the deep infrared source count distribution by the James Webb Space Telescope could reveal the existence of this population of high-redshift star-forming and accreting PBH DM.

Finally, by employing the formalism of Hasinger (2020), we show that if a fraction of accreting PBHs similar to that observed in AGNs in the local universe are radio loud, this model can easily reproduce the enhancement of radio background at high redshifts required to explain the EDGES

21 cm trough result, which is a fraction of the current RSB level in the universe.

4.14. Background of Radio Photons from Primordial Black Holes—Shikhar Mittal

Feng & Holder (2018) first showed that a radio background can enhance the 21 cm signal and potentially explain the amplitude depth seen in the EDGES (Bowman et al. 2018) measurement. We consider accreting PBHs as the originator of the RSB as discussed in Mittal & Kulkarni (2022a).

PBHs are interesting DM candidates formed in the early universe by a gravitational collapse of overdense regions. They are predicted to exist over a wide range of masses. Current observations put constraints in the mass range $\sim 10^{-18}$ – $10^{21} M_{\odot}$ (Carr & Kuhnel 2022). Black holes of masses a few orders of magnitude higher than M_{\odot} are important for studying accretion phenomenon. These black holes are comparable in mass to the astrophysical supermassive black holes that reside in the centers of galaxies and power active galactic nuclei.

Accreting objects generate strong relativistic jets that span a wide range of frequencies in the electromagnetic spectrum. The synchrotron mechanism (Begelman et al. 1984) along with first-order Fermi acceleration (Bell 1978a, 1978b) predict the radio emissivity from accretion jets to follow a power law of index ≈ -0.6 . The resulting excess sky brightness temperature has a power-law dependence on frequency, $T_b \propto \nu^{\beta}$, where $\beta = -2.6$, which is the same as the index reported by ARCADE 2/LWA1. This makes radio-emitting accreting PBHs well-motivated candidates as the generator of the RSB.

The number density of accreting black holes times the luminosity from a single accreting black hole gives an estimate of the total emissivity. Number density can be calculated, assuming a monochromatic mass function and a homogeneous distribution of PBHs, from the mass density of PBHs, which in turn can be written as a fraction f_{PBH} of DM mass density. The single black hole radio luminosity can be calculated from an empirical relation, the so-called fundamental plane of black hole activity, which connects radio luminosity, X-ray luminosity, and the black hole mass. One such relation is provided by Wang et al. (2006) calibrated at a radio frequency of 1.4 GHz and total X-ray luminosity for photon energies in the range 0.1–2.4 keV. In order to model the X-ray luminosity we assume that it is a fixed fraction ($f_X \sim 0.1$) of the bolometric luminosity, which in turn is a fraction λ (Eddington ratio) of the Eddington luminosity. Assuming that a probability f_{duty} (duty cycle) for the black hole to be actively accreting at a particular time, we have at least two free handles to change in order to get the correct radio brightness temperature. Our final expression for comoving radio emissivity due to accreting

PBHs is

$$\epsilon_{\text{acc}}(E) = 5.65 \times 10^{19} f_{\text{duty}} (f_X \lambda)^{0.86} \left(\frac{f_{\text{PBH}} \rho_{\text{DM}}}{1 \text{ kg m}^{-3}} \right) \times \left(\frac{E}{5.79 \text{ } \mu\text{eV}} \right)^{-0.6} \text{ s}^{-1} \text{ m}^{-3}, \quad (7)$$

where ρ_{DM} is the mass density of DM today. We sum the emission—accounting for the cosmological redshift—starting from the epoch photons have been propagating freely, which we assume to be the last scattering of the CMB, i.e., $z_0 \sim 1000$. The resulting radio background specific intensity is

$$J_{\text{acc}}(E, z) = \frac{c}{4\pi} (1+z)^3 \int_z^{z_0} \frac{\epsilon_{\text{acc}}(E')}{1+z'} \frac{dz'}{H(z')}, \quad (8)$$

where $E' = E(1+z')/(1+z)$ and H is the Hubble function. As we are interested in observations made today, we put $z = 0$.

For currently the strongest constraint ($f_{\text{PBH}} \sim 10^{-4}$) obtained by dynamical effects (in particular by halo dynamical friction) on accreting supermassive PBHs of mass $\sim 10^8 M_{\odot}$ (Carr & Sakellariadou 1999; Carr & Kuhnel 2022), and $\lambda = 0.5$, $f_{\text{duty}} = 0.05$ (Shankar et al. 2008; Raimundo & Fabian 2009), we get the net brightness temperature as shown by the blue solid curve in Figure 12. The blue dotted curve shows the ARCADE 2 result (Equation (1)). Within the uncertainties of the free parameter, for $\lambda = 0.1$, $f_{\text{duty}} = 0.01$, we get 5% of ARCADE 2 radio emission, which is necessary to obtain the depth in the EDGES measurement of the 21 cm signal (Mittal et al. 2022).³⁰ The dotted red curve shows the level of radio background required for EDGES, and the solid red curve shows the net brightness temperature from accreting PBHs for lower values of λ and f_{duty} . In both cases, the solid and dotted curves are in excellent agreement with each other as expected since the synchrotron radiation from jets follow a power law of index the same as that reported by observations for frequencies in the radio band.

An obvious question for the scenario discussed here is whether it is allowed by constraints from measurements of the X-ray background and the constraints on reionization. Unfortunately, computing the contribution of the accreting PBHs discussed here to the X-ray background and reionization requires making several poorly understood assumptions all the way to $z \sim 1000$. Nonetheless, with a naive application of our low-redshift understanding of AGN spectral energy distributions to the accreting PBHs, we find that the model can evade the X-ray constraints if the accreting PBHs have a radio-loud fraction similar to AGN. The accreting PBHs also evade reionization constraints if they have obscuration fractions similar to those of AGNs.

³⁰ Along with an enhanced Ly α coupling (Mittal & Kulkarni 2020), though not sufficient to explain the shape of the EDGES profile as explained by Mittal & Kulkarni (2022b).

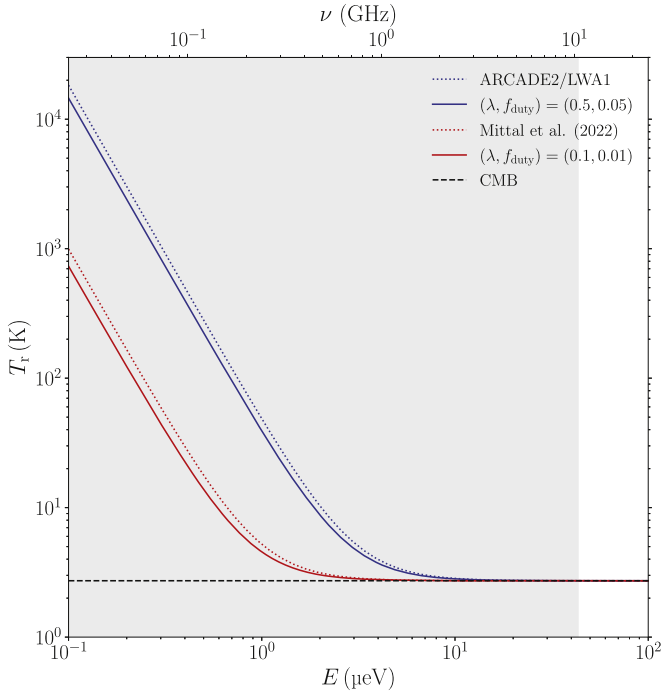


Figure 12. The net background temperature ($T_r = T_b + T_{\text{CMB}}$) generated by radio emission due to accretion onto supermassive PBHs. For $\lambda = 0.5$, $f_X = 0.1$, $f_{\text{duty}} = 0.05$, and $f_{\text{PBH}} = 10^{-4}$ (solid blue), we can explain the RSB observed (dotted blue). For $\lambda = 0.1$, $f_{\text{duty}} = 0.01$ we get (solid red) 5% of ARCADE 2 (dotted red) radio emission necessary to get the EDGES result (Mittal et al. 2022). The CMB temperature is shown in dashed black for reference. The gray shaded region roughly covers the frequency range over which an RSB has been seen.

4.15. Can the Local Bubble Explain the Radio Background?—Martin Krause

The Local Bubble is a low-density cavity in the interstellar medium around the solar system (e.g., Cox & Reynolds 1987), likely formed by winds and explosions of massive stars (Breitschwerdt et al. 2016; Schulreich et al. 2018). Hot gas in the bubble contributes significantly to the soft X-ray background (e.g., Snowden et al. 1997, 1998). The boundary is delineated by a dusty shell (Lallement et al. 2014; Pelgrims et al. 2020) and groups/associations of young stars (Zucker et al. 2022). The superbubble contains high-ionization species (Breitschwerdt & de Avillez 2006) and filaments and clouds of partially neutral and possibly even molecular gas (e.g., Redfield & Linsky 2008, 2015; Snowden et al. 2015; Gry & Jenkins 2017; Linsky et al. 2019) and is threaded by magnetic fields (e.g., Andersson & Potter 2006; McComas et al. 2011; Frisch et al. 2015; Alves et al. 2018; Piirola et al. 2020). The leptonic cosmic-ray distribution is directly measured with near-Earth detectors (e.g., Aguilar et al. 2019). The Local Bubble hence contributes to the radio synchrotron background.

As a guidance for the general distribution of the radio emission in the superbubble, one could take the nonthermal superbubble in IC 10 (Heesen et al. 2015), a smooth, round, and filled structure without edge brightening, that would produce the correct spectrum for the synchrotron background and more than enough flux when scaled to the Local Bubble.

Thanks to a number of measurements unique to the Local Bubble, it is possible to predict its radio emission fairly precisely. Cosmic-ray electrons are directly measured with the Alpha Magnetic Spectrometer on board the International Space Station (Aguilar et al. 2019). Low-energy cosmic rays are inhibited in their propagation through the solar system by the magnetic field of the solar wind. Constraints at lower energy and outside the volume influenced by the solar wind by Voyager I (Cummings et al. 2016) allow for the solution of the propagation problem and thus to derive the particle energy spectrum for the local interstellar medium, i.e., the Local Bubble (Vittino et al. 2019): $n(E) \propto E^{-p}$, with $p = 1.4$ (3.1) below (above) 1 GeV.

The magnetic field in the Local Bubble is constrained by measurements of the Faraday effect (e.g., Xu & Han 2019). Eight pulsars located near the edge of the Local Bubble, all in one particular sector, show an rms rotation measure of 33 rad m^{-2} (Xu & Han 2019). Their mean dispersion measure indicates a column density of free thermal electrons of $N_e = (1.3 \pm 0.6) \times 10^{24} \text{ m}^{-2}$. X-ray measurements of the hot bubble plasma suggest a thermal electron density of $n_{e,X} = (4.68 \pm 0.47) \times 10^3 \text{ m}^{-3}$ (Snowden et al. 2014), typical for superbubbles (Krause et al. 2013, 2014). Warm clouds are observed within the Local Bubble. They have sizes of several parsecs and electron densities of the order of $n_{e,wc} = 10^5 \text{ m}^{-3}$ (e.g., Gry & Jenkins 2017; Linsky et al. 2019). Pressure balance with the volume-filling X-ray plasma generally suggest $\approx 0.5 \text{ nT}$ for warm clouds in the Local Bubble (Snowden et al. 2014). Such data allow estimates of the rotation measure contributions (Krause & Hardcastle 2021 for details). The bulk of the rotation measure is clearly not contributed by warm clouds. It could come from unknown fractions from the bubble wall and hot X-ray plasma inside the bubble, which limits the magnetic field to about 10 nT (100 μG).

A normal turbulent cascade wipes out large-scale fluctuations of the magnetic field over time, unless the magnetic energy density dominates, in which case fluctuations on large scales are built up (inverse cascade; e.g., Christensson et al. 2001; Brandenburg et al. 2015; Sur 2019). One can thus estimate the magnetic field strength from the geometry of the magnetic field, which is constrained by starlight polarization (Berdyugin et al. 2014; Pelgrims et al. 2020). Some coherent large-scale structure seems to be associated with the edge, whereas the interior of the Local Bubble appears to have a magnetic field structure characterized by decaying turbulence, with the largest magnetic filaments about 40 pc long. If this is true, turbulence theory predicts that the magnetic energy

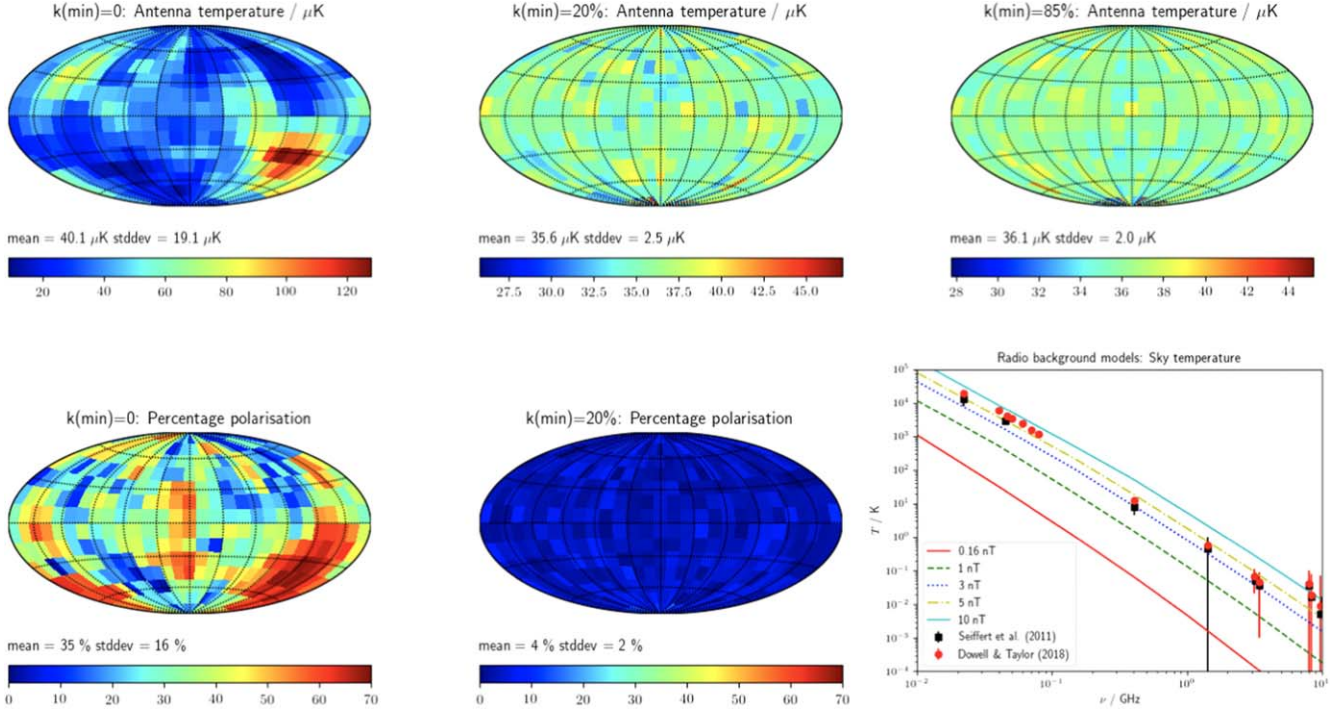


Figure 13. Synthetic radio sky with a mean magnetic field of 1.6 nT at 3.3 GHz (except: bottom right). The resolution is 12° matching that of the ARCADE 2 radiometer. The top row shows the distribution of the antenna temperature. The bottom row shows the fractional polarization for the corresponding image. The left column is for a complete Kolmogorov power spectrum. The middle (right) one is for a model with the 20 (85)% largest modes set to zero. Bottom right: predicted radio synchrotron emission for the Local Bubble for the 85% largest modes set to zero and different mean magnetic field strengths between 0.16 and 10 nT. Measurements are from Seiffert et al. (2011) and Dowell & Taylor (2018). Reproduced from Krause & Hardcastle (2021).

density is not the dominant one in the Local Bubble (compare above).

The magnetic field strength for equipartition between magnetic and thermal energy, is $B_{\text{eq,th}} = 0.61$ nT (Snowden et al. 2014). Equipartition with the energy density in relativistic leptons in our Local Bubble model is reached for $B_{\text{eq,rel}} = 0.16$ nT, a value that would also allow us to interpret the break in the electron energy distribution at 1 TeV as due to synchrotron cooling (López-Coto et al. 2018).

Decaying turbulence is expected in the Local Bubble, as the last supernova happened about 1.5–3.2 Myr ago, as evidenced by deposits of radioactive ^{60}Fe in deep sea sediments (Wallner et al. 2016). This corresponds to at least one sound crossing time through the Local Bubble, which is the characteristic decay time for turbulence. The picture is, however, complicated by the discovery of TeV electrons, which likely point to current energy injection by a pulsar wind (López-Coto et al. 2018; Bykov et al. 2019).

We model the magnetic field in the Local Bubble as a random field with a vector potential drawn from a Rayleigh distribution with a Kolmogorov power spectrum following, e.g., Tribble (1991) and Murgia et al. (2004). We use magnetic field cubes with 256 cells on a side. Following the experimental data on the field geometry, we set the 85% largest modes to

zero. We have also run models for the uncut power spectrum and for a cut at 20% for comparison. We put the observer in the center of the data cube, scale the magnetic field to values within the range allowed by observations and assume a homogeneous distribution of synchrotron-emitting leptons, distributed in energy space according to the model of Vittino et al. (2019). From this setup, we compute radio synchrotron flux and polarization according to standard formulae (see Krause & Hardcastle 2021 for details).

Synthetic antenna temperature and polarization maps are shown in Figure 13. There is little difference between the sky distributions predicted for $k_{\text{min}} = 20\%$ and $k_{\text{min}} = 85\%$. In both cases, the distribution is smooth across the sky with maximum antenna temperature ratios below 2 for any two sky directions and a standard deviation of less than 10% of the mean. A noteworthy polarization signal is only predicted for the full Kolmogorov power spectrum.

The Local Bubble has approximately a power-law radio spectrum very similar to that of the radio background (spectral index $\alpha \approx 0.6$, Figure 13; bottom right). Good agreement with the RSB level is found for magnetic field strengths between 3 and about 5 nT. While such a high magnetic field would be allowed by the pulsar rotation measures, as argued above, it would lead to a dominant magnetic energy density, hence to an

inverse cascade. Apart from the fact that such high magnetic fields are generally not observed in the interstellar medium and that the expected large-scale fluctuations in the starlight polarization are not seen, this would also contradict the observations of the low polarization of the RSB.

The most likely conclusion from this study is hence that the magnetic field in the Local Bubble is low, likely roughly in equipartition with the thermal energy density or the one in relativistic particles. In this case, the Local Bubble can only contribute at the few percent level to the RSB.

4.16. Synchrotron Polarization as a Test of the Radio Background—Al Kogut

The spectral dependence of the observed radio excess, $T_A \propto \nu^\beta$ with $\beta = -2.58 \pm 0.05$ (Fixsen et al. 2011; Dowell & Taylor 2018) is nearly identical to known Galactic features and is highly suggestive of synchrotron emission. Polarization provides a test of Galactic versus extragalactic origin. Synchrotron emission is inherently highly polarized; emission from a single isotropic region with a uniform magnetic field and cosmic-ray energy distribution $N(E) \propto \kappa E^{-p}$ will have spectral index $\beta = -(p+3)/2$ and fractional polarization $f = \frac{p+1}{p+7/3}$ (Rybicki & Lightman 1979). The observed spectral index implies $p = 2.2$ and fractional polarization as high as $f \sim 0.7$.

The actual microwave sky, in contrast, is strikingly depolarized. Figure 14 shows the polarized intensity $P = (Q^2 + U^2)^{1/2}$, polarization angle $\psi = 0.5 \arctan(Q/U)$, and fractional (polarization $f = P/I$ for the Planck synchrotron model; Adam et al. 2016; Akrami et al. 2020) evaluated at a frequency of 30 GHz, where I, Q, U are the Stokes parameters. Two features are evident. Although synchrotron emission is nominally highly polarized, 50% of the sky at Galactic latitude $|b| > 20^\circ$ has a fractional polarization $f < 0.031$. Despite this, the polarization direction is highly organized, with little scatter in polarization direction from neighboring pixels. We quantify this by computing the difference in polarization angle between each pixel and its neighbors, $\Delta\psi = \sum_j (|\psi_i - \psi_j|)$ and find a median value $\Delta\psi = 14^\circ$ at $|b| > 20^\circ$.

These two features are difficult to reconcile. Depolarization from multiple independent domains along individual lines of sight should also affect the polarization angle $\psi(\hat{n})$ in each line of sight \hat{n} . Since depolarization is a random process, the scatter in polarization angle from one line of sight to another should increase as additional independent domains align in different directions.

Magnetohydrodynamic (MHD) simulations allow a simultaneous assessment of both depolarization and alignment. We use the Enzo code (Collins et al. 2010; Bryan et al. 2014) to generate realizations of a turbulent magnetic field within a 512^3 data cube. We begin with cubes of uniform density and constant magnetic field $\mathbf{B}_0 = B_0 \hat{x}$, then add kinetic energy on

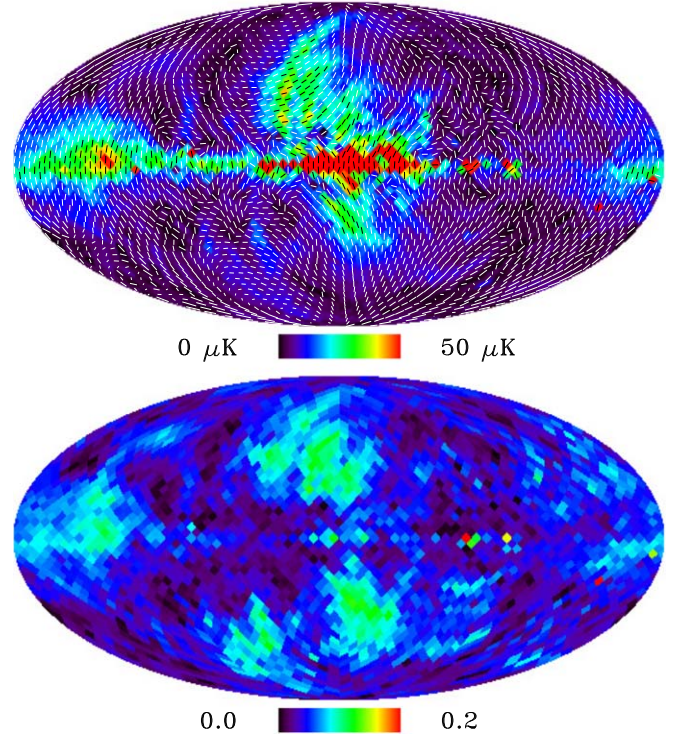


Figure 14. Polarization intensity P (top) and fractional polarization P/I (bottom) from Planck evaluated at 30 GHz. Despite the high degree of depolarization, the polarization angle (white bars) shows little scatter.

large scales. The MHD equations cascade the energy from the large injection scales to progressively smaller-scale structures, tangling the magnetic field in a physically accurate fashion (Collins et al. 2010). The ratio of the mean magnetic field to tangled magnetic field is determined by the ratio of thermal, kinetic, and magnetic energies, which we vary over a grid in the sonic Mach number $M = v_{\text{rms}}/c_s$ and the Alfvén Mach number $M_A = v_{\text{rms}}/v_A$, with c_s the speed of sound in the medium and v_A the speed of an Alfvén wave in the medium. For each pair of Mach numbers, we use the resulting 3D magnetic field to evaluate the synchrotron emission vector within each cube cell, then sum the emission along each of the cube faces to evaluate the projected synchrotron emission in polarization and intensity perpendicular and parallel to the input field.

Table 3 shows the results. None of the simulations simultaneously reproduce both the Planck fractional polarization and angular scatter. The lowest fractional polarizations from the simulations ($f = 0.06$) are seen for the face parallel to the ordered field but the corresponding angular scatter for this face ($\Delta\psi = 49^\circ$) shows a near-complete lack of angular correlation. Conversely, simulations viewed along the perpendicular faces show angular scatter roughly compatible with the

Table 3
MHD Simulation Results

Mach Number		Parallel to \mathbf{B}_0		Perp. to \mathbf{B}_0	
M	M_A	f	$\Delta\psi$ ($^\circ$)	f	$\Delta\psi$ ($^\circ$)
0.5	0.5	0.33	40.0	0.68	1.6
0.5	2.0	0.06	49.0	0.09	11.0
1.0	0.5	0.34	43.0	0.69	1.7
1.0	2.0	0.10	40.0	0.13	10.0
2.0	2.0	0.17	38.0	0.23	9.0
3.0	2.0	0.17	42.0	0.21	9.5
Planck (nominal) $f = 0.031$ and $\Delta\psi = 14^\circ 1$					
Planck (corrected ^a) $f = 0.144$ and $\Delta\psi = 14^\circ 1$					

Note.

^a After removing monopole component (see text).

Planck model but now with fractional polarization a factor of 3 or more higher than observed.

An extragalactic radio background can mitigate this tension. If some or all of the observed radio monopole component is extragalactic, it should be removed from the Galactic synchrotron model prior to computing the fractional polarization. The Planck synchrotron model applies a correction for the integrated emission of extragalactic radio sources, but this accounts for less than a quarter of the total radio monopole component. Subtracting the entire radio monopole component from the Planck model of unpolarized synchrotron emission increases the median fractional polarization without affecting the scatter in polarization angles. The median values $f = 0.14$ and $\Delta\psi = 14^\circ$ after monopole subtraction are now compatible with the range of MHD simulations.

4.17. Strategies to Identify the Galactic Foreground— Isabella P. Carucci

This talk summarized the strategies for identifying an astrophysical background in HI Intensity Mapping (IM). The contribution to the workshop discussion was twofold. (i) To present the HI IM observable, which constitutes a novel kind of data in the radio band, and (ii) to illustrate the ongoing efforts to characterize the foregrounds of HI IM, focusing on the statistical techniques that are crucial in the characterization of weak signals and with promising applications to RSB science.

HI resides abundantly in all galaxies and shines in the 21 cm line hyperfine transition. Therefore, it is a perfect candidate for mapping the universe’s large-scale structure. However, the line’s weakness prohibits the use of traditional surveys targeting galaxies for covering large areas and deep redshifts necessary for cosmological studies. To overcome this issue, we use the IM technique: Instead of resolving individual sources, we collect all their integrated emission, scanning large portions

of the sky quickly and economically and, at the same time, preserving the accurate redshift information from the 21 cm spectral line.

HI IM is an emerging science area; many are the new or planned instruments that can perform such surveys, such as the Canadian Hydrogen Intensity Mapping Experiment (CHIME—e.g., Amiri et al. 2022), Baryon Acoustic Oscillations from Integrated Neutral Gas Observations (BINGO—e.g., Abdalla et al. 2022), Hydrogen Intensity and Real-time Analysis eXperiment (HIRAX—e.g., Crichton et al. 2022), Tianlai (e.g., Wu et al. 2021), MeerKAT (e.g., Wang et al. 2021), and eventually SKAO. HI IM will bring new radio data in the 100 MHz–1 GHz regime. Although no experiments plan to achieve absolute calibration as HI IM looks after temperature fluctuations, new radio data on a significant fraction of the sky means further information on, e.g., the diffuse galactic synchrotron radiation (Irfan et al. 2022), the galactic magnetic field, and extragalactic emissions.

Despite its promising science, HI IM measurements face formidable challenges, as shown in its first application in cross-correlation with galaxies (Chang et al. 2010)—no direct detection has been performed yet. The main reason is the presence of not-well-characterized contaminants: Foregrounds of astrophysical origin are orders of magnitude more intense than the signal (Alonso et al. 2014). Moreover, this substantial difference in intensity among components translates any possible tiny leakage due to the instruments’ imperfections and calibration uncertainties into catastrophic contamination, which is hard to model or prevent (e.g., Shaw et al. 2015).

Given the gravity of the cleaning problem, the community addresses it with Blind Source Separation (BSS) methods. The two main BSS strategies are Principal Component Analysis (PCA) and Independent Component Analysis (ICA)—i.e., assuming the signal components are uncorrelated or statistically independent. Their application to data has been successful, especially on cross-detection with a second galaxy catalog (e.g., Masui et al. 2013; Switzer et al. 2013; Cunnington et al. 2023; Wolz et al. 2022). However, we are improving the standard BSS techniques and optimizing them to our specific scope. In particular, we have recently devised a new component separation method named mixGMCA. It is a hybrid PCA and sparsity-based Generalized Morphological Component Analysis (GMCA—e.g., Bobin et al. 2007) BSS algorithm that uses wavelet decomposition of the maps and different treatments of their large and small spatial scales. GMCA assumes that the foreground components verify two hypotheses: sparse in a given domain (i.e., most samples are zero-valued) and morphologically diverse (their non-zero samples appear at different locations), easing their separation, which we achieve through a minimization problem. Carucci et al. (2020) demonstrated the wavelets to be optimal to describe the HI IM foreground components sparsely and highlighted how the sparse assumption holds better at small

rather than large spatial scales. Since the wavelet decomposition offers a direct framework for analyzing multiscale data, we started allowing different mixtures and components to describe the signal at different scales. In practice, mixGMCA applies PCA on the largest scale³¹ and GMCA on the remaining ones. Then, it assembles the two solutions before retransforming the maps into pixel space. mixGMCA participated in the first Blind Foreground Subtraction Challenge of the SKA Cosmology Science Working Group (Spinelli et al. 2022). Results are promising: mixGMCA effectively removes the brightest diffuse astrophysical emissions with PCA while carefully handling the small-scale instrument-driven defects in the maps with GMCA. We are now testing mixGMCA on MeerKLASS data (Wang et al. 2021).

Component separation techniques are ubiquitous in data analysis. In particular, sparsity-based statistical learning algorithms have already been successfully applied in several astrophysical contexts, for example, CMB (Bobin et al. 2014), high-redshift 21 cm interferometry (Patil et al. 2017), and X-ray images of supernova remnants (Picquenot et al. 2019). The component separation efforts we are conducting in the HI IM context could be significant in the measurements proposed during the workshop: (i) the radio SZ effect (discussed in Section 4.9), and (ii) cross-correlation analyses (discussed in Section 5). Indeed, regarding the SZ effect, characterizing the halos, radio relics, and all structured components from the background is challenging, with higher chances of being achieved through the appropriate statistical methods as those here overviewed.

4.18. Characterization of the Diffuse Radio Sky with EDGES and MIST—Raul Monsalve

Understanding the origin of the radio synchrotron background requires accurate absolutely calibrated sky maps made at many frequencies over a wide frequency range. This talk focused on the efforts from the EDGES and MIST experiments to provide accurate absolute calibration to existing maps below 160 MHz, which complements the work to produce new maps with intrinsically better calibration (Sections 4.1 and 4.2). The talk also described other ways in which EDGES and MIST are contributing to the characterization of the radio sky.

EDGES: The Experiment to Detect the Global EoR Signature (*EDGES*)³² employs single-antenna, wideband, total-power radiometers measuring over the range 45–200 MHz to attempt to detect the highly redshifted 21 cm signal from the cosmic dawn and the Epoch of Reionization at redshifts $30 \gtrsim z \gtrsim 6$. *EDGES* is located at the Murchison Radioastronomy Observatory (MRO) in Western Australia at a latitude of -26.97 . Since 2008 *EDGES* has contributed to the

characterization of the diffuse Galactic and extragalactic synchrotron radiation, which is the main foreground in measurements of the high-redshift 21 cm signal (Rogers & Bowman 2008; Mozdzen et al. 2017, 2019).

In Monsalve et al. (2021), we reported the absolute calibration of two low-frequency maps using *EDGES* measurements. The maps are (1) from Guzmán et al. (2011) at 45 MHz, produced by combining the original maps by Alvarez et al. (1999) at 45 MHz and Maeda et al. (1999) at 46.5 MHz; and (2) from Landecker & Wielebinski (1970) at 150 MHz, which combines their own 150 MHz observations with maps from Yates et al. (1967) at 85 MHz and Turtle & Baldwin (1962) at 178 MHz. To calibrate the 45 MHz map, we used data from two *EDGES* low-band instruments (Bowman et al. 2018), which, although identical in principle, are observed on the sky with their dipole antennas at azimuthal orientations $\approx 90^\circ$ apart. The absolute noise temperature calibration of *EDGES* is provided by laboratory measurements of resistive loads at ≈ 300 and 400 K connected at the input of the instrument in place of the antenna. To obtain our results, we simultaneously fitted both *EDGES* low-band data sets to simulated observations produced by convolving the Guzmán et al. (2011) map with models of the *EDGES* low-band antenna beam. Our model for the calibrated map is $k_1 \times \text{input map} + k_2$, and the best-fit parameters found for the the Guzmán et al. (2011) map are $k_1 = 1.076 \pm 0.034$ (2σ) and $k_2 = -160 \pm 78$ K (2σ). Our results account for systematic uncertainties from receiver calibration, antenna orientation, ground properties, ionospheric and tropospheric effects, as well as from the choice of using a single data set in the analysis instead of both simultaneously. When this calibration is applied to the map, the brightness temperature at the reference Galactic coordinates $(l, b) = (+190^\circ, +50^\circ)$ —in the region of lowest temperature in the sky—goes from $3326 \pm \gtrsim 333$ K in the input map to 3419 ± 255 K (2σ) in the calibrated map. To calibrate the Landecker & Wielebinski (1970) 150 MHz map, we used data from *EDGES* high-band (Mozdzen et al. 2017) and midband, whose horizontal blade dipole antennas are oriented $\approx 90^\circ$ apart. Beyond the antenna orientations, the high- and midband systems are different in antenna size, ground plane size and shape, bandwidth, and receiver electronics. The results for this map are $k_1 = 1.112 \pm 0.023$ (2σ) and $k_2 = 0.7 \pm 6.0$ K (2σ), and the brightness temperature of the map at Galactic coordinates $(l, b) = (+190^\circ, +50^\circ)$ goes from $148.9 \pm \gtrsim 41$ K in the input map to 166.3 ± 14.3 K (2σ) in the calibrated map.

Currently, we are working to provide absolute calibration to the 159 MHz map recently published by Kriele et al. (2022) from data obtained with the EDA2 SKA-Low prototype. For this, we are using observations with the same *EDGES* high- and midband blade dipole antennas as for the Landecker & Wielebinski (1970) map and also observations from an earlier version of the high-band instrument, which measured with a

³¹ The coarse approximation of the maps resulting from the initial low-pass filtering of the wavelet decomposition.

³² <https://loco.lab.asu.edu/edges/>

Fourpoint antenna (Mozdzen et al. 2016). Preliminarily, we find that the results from each of the individual data sets are very consistent, which represent strong validation of our understanding of the different instruments (R. Monsalve et al. 2023, in preparation). EDGES has also recently reported the detection of $H\alpha$ and $C\alpha$ radio recombination lines (RRLs) in sky-average observations with the low-band and midband instruments. The detections occur across the full range of sidereal time although, as expected, their absolute amplitudes decrease toward high Galactic latitudes. Of particular interest is the report of the upper limit 33 ± 11 mK (1σ) for the absorption amplitude of the $C\alpha$ line at high Galactic latitudes when stacking all the expected RRL frequencies in the range 50–87 MHz.

MIST: The Mapper of the IGM Spin Temperature (*MIST*)³³ is a new experiment to detect the global high-redshift 21 cm signal, which has been designed to be portable and power efficient in order to conduct observations from several remote locations around the world. The instrument corresponds to a single-antenna total-power radiometer, which, although similar, is different from EDGES in several ways. The main difference is that *MIST* does not use a metal ground plane in order to avoid potential systematic effects due to unaccounted-for interactions with the antenna and the soil. In 2022 May, test measurements with *MIST* were conducted from the Deep Springs Valley, California, and the Death Valley, Nevada (see Figure 15). These measurements were very successful and are currently being analyzed to determine the contribution of the sky-averaged radio synchrotron emission in the northern hemisphere as well as the full effect of the ground on the sky measurements. Finally, given the success of the California and Nevada measurements, *MIST* planned to conduct observations from the Canadian High-Arctic, at a latitude of $\approx +79^\circ.5$, in 2022 July. This site is excellent in terms of its radio-quiet conditions (Dyson et al. 2021) as well as in terms of the characteristics of the ground.

4.19. Impact of Radio Background on the High-redshift 21 cm Signal—Anastasia Fialkov

The redshifted 21 cm signal of neutral hydrogen (e.g., Furlanetto et al. 2006; Barkana 2016; Mesinger 2019) can be described as a spectral distortion of the radio background spectrum, which is typically assumed to be the CMB. This signal is imprinted onto the radio background as it propagates through neutral high-redshift hydrogen gas. Radio photons at the intrinsic 1.42 GHz frequency are absorbed/emitted by hydrogen atoms if the characteristic temperature of the 21 cm transition, T_S , is colder/hotter than the temperature of the background radiation, T_{rad} . If the radio background has an excess contribution in addition to the CMB, this will be

³³ <http://www.physics.mcgill.ca/mist/>



Figure 15. *MIST* instrument conducting test observations in Deep Springs, California (top), and in Death Valley, Nevada (bottom) in 2022 May. *MIST* is a single-antenna total-power radiometer without a metal ground plane. The antenna is a blade dipole of 2.4 m tip-to-tip length and the measurements span the 25–125 MHz range. These test measurements are currently being analyzed to understand the diffuse synchrotron emission in the northern hemisphere as well as the effect of the ground on the sky measurements.

manifested in the shape of the spectral distortion. Therefore, the 21 cm signal can be used to test cosmic origin of the observed RSB (e.g., Fialkov & Barkana 2019; Reis et al. 2020a). The distortion is imprinted at the intrinsic frequency, corresponding to the wavelength of 21 cm, but due to the expansion of the universe it is observed at a frequency lower by a factor $1 + z$, where z is the redshift of the hydrogen cloud. For cosmological redshifts corresponding to the Epoch of Reionization (EoR) and cosmic dawn, $z \sim 5\text{--}50$, the signal is imprinted at frequencies below 200 MHz and can be detected by low-frequency radio telescopes such as HERA (Abdurashidova et al. 2022), LOFAR (Mertens et al. 2020), MWA (Ewall-Wice et al. 2016), EDGES (Bowman et al. 2018), and SARAS (Singh & Subrahmanyan 2019; Singh et al. 2022).

First proposed by Feng & Holder (2018), the impact of the the excess radio background on the 21 cm signal was

extensively modeled in later works (Ewall-Wice et al. 2018; Mirocha & Furlanetto 2018; Fialkov & Barkana 2019; Reis et al. 2020a). The main effects include a boost in the contrast between T_S and T_{rad} , which leads to a deeper 21 cm absorption trough, a weaker coupling between T_S and the gas kinetic temperature, T_K , and an enhancement of the radiative heating (e.g., Fialkov & Barkana 2019). Effectively, excess radio background over the CMB slows down the cosmic clock of the 21 cm signal. With an excess radio background it takes longer for the astrophysical processes (described below) to affect the 21 cm signal (Reis et al. 2020a). Therefore, an enhanced radio background might have important implications for 21 cm cosmology.

The signature of the excess radio background is partially degenerate with astrophysical effects. The 21 cm signal is a probe of the thermal and ionization states of the intergalactic medium (IGM) and thus can be used to constrain the formation of the first stars and galaxies (see, e.g., Furlanetto et al. 2006; Barkana 2016; Mesinger 2019). As these first sources of radiation appear, their light affects the 21 cm signal via a number of processes. Arguably, the most important effect is coupling of T_S to T_K by stellar Ly α photons (the Wouthuysen–Field, WF, effect, Wouthuysen 1952; Field 1958). It is owing to this effect that the 21 cm signal is observable against the background radiation. The strength and exact redshift of the signal imprinted by the Ly α photons depend on the properties and formation time of the very first stars.

The next major component that determines the shape of the distortion is the gas kinetic temperature. At cosmic dawn, the thermal evolution is driven by adiabatic cooling, T_K is lower than T_{rad} , and the 21 cm signal is seen in absorption. X-ray radiation produced by the first population of X-ray binaries heats up the gas. We assume that X-ray luminosity scales with star formation rate and introduce a free scaling parameter f_X that can be constrained with data. If as a result of this heating T_K exceeds T_{rad} , the 21 cm signal will be seen in emission at the EoR (Fialkov et al. 2014). Ly α and radio photons also contribute to heating the gas (Venumadhav et al. 2018; Reis et al. 2020b), but in most plausible scenarios their contribution is subdominant to that of X-rays.

In our recent works we have considered two types of excess radio backgrounds and their impacts on the 21 cm signal. In Fialkov & Barkana (2019), we focused on a phenomenological synchrotron radio background (motivated by the ARCADE 2 and LWAl measurements), which adds a homogeneous contribution to the high-redshift T_{rad} that decays with time, while in Reis et al. (2020a) we considered a radio background produced by a growing population of radio galaxies. Such a radio background exhibits fluctuations that trace the nonhomogeneous star formation. The strength of radio emission produced by a star-forming region scales with star formation rate multiplied by a free scaling factor f_{Radio} , which can be constrained using data. The average value of f_{Radio} in

star-forming galaxies today is $f_{\text{Radio}} = 1$. We calculate the temperature of the radio background by integrating over the contribution of all galaxies within the past light cone.

For extreme values of f_{Radio} ($f_{\text{Radio}} > 300$; e.g., Reis et al. 2020a), the excess radio background created by galaxies can explain the anomalously deep (and yet unverified) sky-averaged 21 cm signal reported by the EDGES collaboration (Bowman et al. 2018). The strong radio background needs to be accompanied by strong X-ray heating and Ly α background to ensure a narrow absorption profile similar to the reported one. Even though the EDGES detection has not been confirmed (e.g., Hills et al. 2018; Singh et al. 2022), the presence of the strong radio background at high redshifts can be tested with other 21 cm experiments that provide upper limits including the interferometers HERA (Abdurashidova et al. 2022), LOFAR (Mertens et al. 2020), and MWA (Ewall-Wice et al. 2016) as well as global signal experiments such as SARAS2 (Bevins et al. 2022) and SARAS3 (Bevins et al. 2023).

Out of the existing limits on the power spectrum, the strongest constraint comes from the HERA measurement at $z = 8$. Comparing our models to this limit, we find constraints on the strength of the radio background and X-ray heating (see Section 8 of Abdurashidova et al. 2022). We rule out (with 95% confidence) the combination of high radio luminosity of high-redshift galaxies of $L_{r,150 \text{ MHz}}/\text{SFR} > 4 \times 10^{24} \text{ W Hz}^{-1} M_{\odot}^{-1} \text{ yr}$ and low X-ray luminosities of $L_{X,0.2-95 \text{ keV}}/\text{SFR} < 7.6 \times 10^{39} \text{ erg s}^{-1} M_{\odot}^{-1} \text{ yr}$. These luminosities correspond to $f_X > 0.25$ and $f_{\text{Radio}} < 397$ constrained at the 68% confidence level individually.

The same measurement can be used to constrain the phenomenological synchrotron background model. Here we find that scenarios with a high excess radio background of $A_r > 31$ (where A_r is the amplitude of the excess radio background relative to the CMB calculated at the reference frequency of 78 MHz assuming $\beta = -2.6$ spectral index), corresponding to 1.6% of the CMB at 1.42 GHz, are excluded at 68% confidence. In a similar manner, models with a low X-ray efficiency of $f_X < 0.20$ (corresponding to the X-ray luminosity per SFR of $L_{X,0.2-95 \text{ keV}}/\text{SFR} < 5.9 \times 10^{39} \text{ erg s}^{-1} M_{\odot}^{-1} \text{ yr}$) are excluded.

Global signal experiments are also delivering constraining data. In disagreement with the EDGES collaboration, which reported the puzzling detection, SARAS2 and SARAS3 experiments put limits on the 21 cm signal from cosmic dawn and the EoR (Singh et al. 2018, 2022). Specifically, SARAS2 takes measurements at $z = 7-12$ while SARAS3 probes the 21 cm signal from $z \sim 15-32$. In agreement with HERA, these measurements disfavor a strong radio background at the EoR and weak X-ray heating (see Bevins et al. 2022 and Bevins et al. 2023). The SARAS experiments probe a much wider redshift range than HERA, thus providing a unique view into the astrophysical processes deep at cosmic dawn.

4.20. A Stimulating Explanation of the Extragalactic Radio Excess—Andrea Caputo

Beyond the standard model (BSM), explanations proposed thus far to solve the radio excess background have primarily focused on synchrotron emission from DM annihilation and decay (Fornengo et al. 2011; Cline & Vincent 2014; Fang & Linden 2015). However, these models typically run into several issues, for example, they may result in nonsmooth emission or underproduce T_{exc} (here defined as the majority of T_{BGND} in Equation (1), which is in excess of that which would result from known source classes), unless the magnetic fields responsible for synchrotron production have unusual properties (Cline & Vincent 2014; Fang & Linden 2015). In Caputo et al. (2022), we have proposed a new simple class of experimentally viable new-physics models that can explain the amplitude, power-law dependence, and smoothness of T_{exc} . These models rely on three basic ingredients: (1) a particle decaying into dark photons A' ; (2) the presence of a thermal bath of A' , which stimulates this decay; and (3) A' resonantly oscillating into radio photons. A particle physics model that has these three features can generate an RSB with $T_{\text{exc}} \propto \omega^{-5/2}$.

There are several parameters that depend on the specifics of the chosen model. In Caputo et al. (2022), the fiducial model involves a DM axion-like particle (ALP) of mass m_a decaying into an A' with energy $\omega_{A'} = m_a/2$, in the presence of a thermal bath of A' , which stimulates the decay due to Bose enhancement, leading to a redshift-dependent effective decay lifetime $\tau(z)$:

$$\tau(z) = \tau_{\text{vac}}[1 + 2f_{A'}^{\text{BB}}(z)]^{-1}, \quad (9)$$

with $f_{A'}^{\text{BB}} = (e^{\omega_{A'}/T'} - 1)^{-1}$ being the blackbody occupation number of A' with energy $\omega_{A'}$ and temperature T' .

Once the A' are produced, they can then oscillate into ordinary photons via the so-called kinetic mixing, ϵ , which enables resonant conversion between the photons and dark photons whenever their masses match $m_{A'}^2 = m_\gamma^2$, where m_γ^2 is the effective photon plasma mass squared. This quantity is proportional to the free electron number density, n_e . The converted photons ultimately form the present-day T_{exc} . We calculate the sky-averaged conversion probability per redshift $\langle dP_{A' \rightarrow \gamma} \rangle / dz$, taking into account inhomogeneities using the formalism developed in Caputo et al. (2020).

All in all, the number density of produced photons within this mechanisms simply reads

$$\frac{dn_\gamma}{dx}(x, z) = \frac{\rho_a(z)}{m_a} \frac{1}{x} \frac{1}{\tau(z_*)} \frac{1}{H(z_*)} \int_z^{z_*} dz' \frac{\langle dP_{A' \rightarrow \gamma} \rangle}{dz'}, \quad (10)$$

$\propto x^{-1} \quad \propto x^{3/2} \quad \propto x^{-1}$

where $\rho_a(z)$ is the DM density at redshift z , $x \equiv \omega/[T_0(1+z)]$, z_* is the redshift at which a daughter A' with frequency ω at redshift z was produced— $1+z_* \equiv \omega_{A'}(1+z)/\omega$ —and we assumed all the decays to happen during matter domination

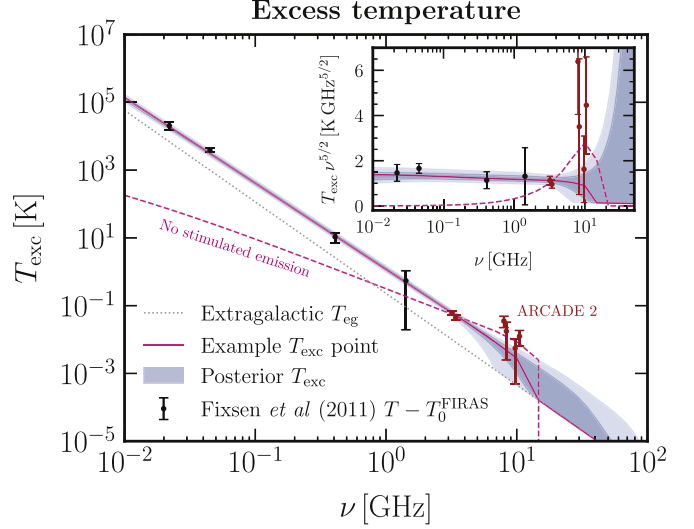


Figure 16. Point-wise posterior for T_{exc} within our proposed model, showing the middle 68% and 95% regions (dark and light blue regions, respectively). We include the contribution from unresolved extragalactic sources T_{eg} (dashed gray—Gervasi et al. 2008) for completeness. The spectrum for a single point in parameter space is shown in pink. Radio data, plotted as $T - T_0^{\text{FIRAS}}$, include measurements from ARCADE 2, shown in red (Fixsen et al. 2011), with results from other telescopes shown in black. The pink dashed line shows a fit to the ARCADE 2 data only assuming no stimulated emission.

(and therefore $H(z_*) \propto x^{3/2}$). This gives $dn_\gamma/dx \propto x^{-3/2}$, or $T_{\text{exc}} \propto \omega^{-5/2}$, the desired frequency dependence.

Using this simple result, we have performed a scan of the model parameter space, individuating the preferred regions which provide a good fit to radio data at all frequencies, while avoiding all other bounds for the considered model. We explored the posterior on the model parameters using nested sampling. Our priors are constructed such that they have zero probability density in parameter regions incompatible with (1) the FIRAS spectral distortion limits of Caputo et al. (2020) and (2) DM lifetime limit (Simon et al. 2022). Priors on T_0' and T_0 are also chosen to account for the number of relativistic degrees of freedom N_{eff} and FIRAS constraints on these parameters, respectively. The posterior on the excess temperature is shown in Figure 16, where we also included an irreducible contribution from unresolved extragalactic radio sources (dashed gray line; Gervasi et al. 2008). We find an excellent fit to the data over a wide range of allowed model parameters.

Finally, as already mentioned, another challenge for models explaining the radio background is its smoothness. There are two possible contributions to the anisotropy produced by our model: (1) decay anisotropy, due to DM density correlations from the point at which a decays, and (2) conversion anisotropy, due to correlations in electron density fluctuations, δ_e , since $m_\gamma^2 \propto n_e$. The decay anisotropy was found to exceed the radio anisotropy power spectrum unless the decay happens

at $z_* \gtrsim 5$ (Holder 2014), a criterion easily satisfied in the range of parameters providing a good fit. We therefore computed the conversion anisotropy power spectrum by first writing down the two-point correlation function of the conversion probability of $A' \rightarrow \gamma$ in two different directions in the sky. Our computation (Caputo et al. 2022) shows that producing a sufficiently smooth radio background is highly plausible within the model and calls for further studies of the two-point function of δ_e (which for simplicity we modeled as either a Gaussian or a log-normal random field).

Future experiments can probe our model. PIXIE (Kogut et al. 2011b) can be sensitive to CMB spectral distortions due to A' and is expected to almost fully cover the 95% region of our posterior distribution in the ϵ - $m_{A'}$ plane. The thermal population of A' may also lead to a value of N_{eff} that is detectable in future CMB experiments such as CMB-S4 (Abazajian et al. 2019).

4.21. WIMP Dark Matter and Radio Correlations—Elena Pinetti

The nature of DM remains a puzzle to date. One enticing possibility is that it is made up of new particles, which may annihilate and produce a huge variety of astrophysical messengers that we can study in order to infer meaningful information on the DM's properties. In Pinetti et al. (2020), we focused on the prompt gamma-ray flux produced by particles with a mass between 10 GeV and 10 TeV, annihilating into $b\bar{b}$ quarks. Astrophysical observations and N -body simulations reveal that DM in the universe is distributed in a hierarchical and anisotropic way. Therefore, we expect that the electromagnetic signals indirectly produced by DM particles will exhibit a certain degree of anisotropy as well (see Fornasa & Sanchez-Conde 2015 for a review). This is particularly interesting considering that the unresolved gamma-ray background (defined as the total gamma-ray flux minus the Galactic plane and the resolved astrophysical sources) is observed to be anisotropic (Ackermann et al. 2012). In Pinetti et al. (2020), we investigated whether there is a correlation between the anisotropies of the gamma-ray sky and a DM signal, taking into account also the presence of the astrophysical background due to the unresolved astrophysical sources (mainly star-forming galaxies and AGNs). We employed the cross-correlation technique, which is a powerful method to estimate the correlation between the fluctuations of a gravitational tracer—which is a manifestation of the existence of DM—and an electromagnetic signal—which is a byproduct of the exotic nature of DM. If we find a positive signal in this cross-correlation channel, we can argue that DM is made up of exotic physics and is not, for instance, the result of an alternative theory of gravity. For the first time we forecasted the cross-correlation signal between the

unresolved gamma-ray background and the distribution of neutral hydrogen, measurable with radio telescopes. Neutral hydrogen atoms produce the 21 cm line via the spin-flip transition from a higher energy level to the ground state. This emission line acts as a promising gravitational tracer, notably in view of the next-generation experiment SKA, which will be the world's largest radio telescope, with over a square kilometer of collecting area (Bacon et al. 2020). The SKA is currently under construction, while its precursors are already taking data, including MeerKAT, which is relevant for this analysis. These radio detectors will be used for 21 cm line intensity mapping: a cutting-edge technique, which consists of measuring the integrated emission of a the 21 cm line, originating from the intergalactic medium and galaxies (Bull et al. 2015). The main advantage of 21 cm intensity mapping is the great redshift resolution, which is a key factor for DM searches, where we expect the low-redshift structures to dominate our DM signal, while the contribution of the unresolved astrophysical sources is peaked at higher redshift (typically between 0.5 and 1). Regarding the gamma-ray emission, we considered Fermi-LAT as the benchmark detectors. We also take into account a next-generation gamma-ray telescope, which we called Fermissimo, with improved exposure and angular resolution. The angular power spectrum is the statistical tool employed to estimate the cross-correlation signal:

$$C_\ell^{\gamma \times \text{HI}} = \int dz \frac{c}{H(z)\chi^2(z)} W_\gamma(z) W_{\text{HI}}(z) P_{\gamma \times \text{HI}} \left(k = \frac{\ell}{\chi(z)} \right) \quad (11)$$

where $W_\gamma(z)$ and $W_{\text{HI}}(z)$ are the two window functions associated to the gamma-ray flux and 21 cm line emission, respectively, and they encoded the information on the redshift evolution of the observables, while $P_{\gamma \times \text{HI}}$ is the Fourier power spectrum. The variance on the $C_\ell^{\gamma \times \text{HI}}$ has been derived under the hypothesis of Gaussianity. The angular power spectrum and its variance have been employed to derive the forecasted bounds on the DM parameter space and determine the opportunities for DM searches offered by radio correlations with next-generation radio telescopes. Figure 17 illustrates the 2σ limits on the velocity-averaged annihilation cross section (vertical axis) as a function of the DM mass (horizontal axis) for different combination of detectors, as indicated in the legend (solid lines). Other constraints are also shown for comparison (see caption for details). The figure shows that the configurations MeerKAT \times Fermi-LAT and SKA1 \times Fermi-LAT are already competitive with current constraints, while Fermissimo would allow to investigate DM masses up to few TeV, with a 5σ detection reach possible for thermal particles with masses up to 400 GeV.

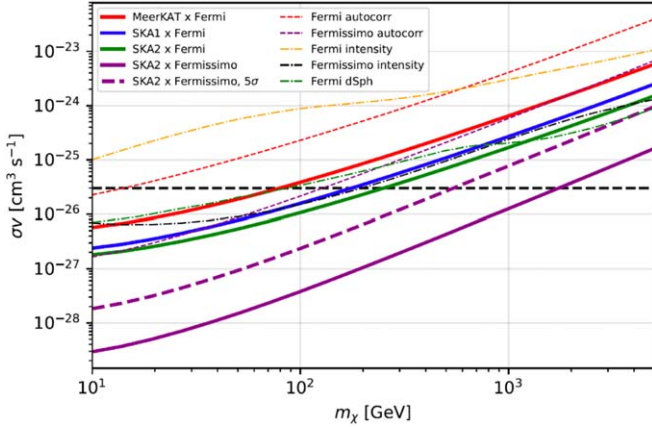


Figure 17. Limits on the cross section as a function of the DM mass. Comparison with limits from autocorrelation of gamma-rays (dashed red for Fermi; Ackermann et al. 2018, light purple dashed for Fermissimo), intensity of the gamma-ray flux (yellow for Fermi Ackermann et al. 2015, black for Fermissimo) and dwarf spheroidal galaxies (Albert et al. 2017).

4.22. Dark Matter Constraints from Planck Observations of the Galactic Polarized Synchrotron Emission— Alessandro Cuoco

High-energetic cosmic-ray (CR) electrons and positrons (e^\pm) can be of astrophysical origin or be produced by the annihilation or decay of DM particles in the halo of DM particles surrounding the Galaxy. They can then propagate in the interstellar Galactic magnetic field (GMF) and produce radio and microwave synchrotron emission. The potential DM synchrotron signal in the Galactic halo and in extragalactic targets has been studied using radio and microwave surveys, such as WMAP and Planck (Delahaye et al. 2012; Egorov et al. 2016; Cirelli & Taoso 2016; Fornengo et al. 2011, 2014; Hooper et al. 2012). These DM studies have typically focused on the total intensity, i.e., the Stokes parameter I . However, synchrotron emission from e^\pm is partially linearly polarized, and a polarization signal (i.e., Stokes P) is thus expected. In Manconi et al. (2022), we have exploited the Planck polarization maps in order to constrain the Galactic DM signal. In the following we will briefly summarize our findings, referring to Manconi et al. (2022) for a more detailed description.

To constrain the DM signal, we will use intensity and polarization maps from the latest Planck data release (Aghanim et al. 2020a) at frequencies of 30, 44, and 70 GHz. Furthermore, we also build the related error maps using a procedure that estimates the variance of the signal in each pixel using the neighboring pixels. At these frequencies, the emission is dominated by the Galactic foregrounds rather than by the CMB. Nonetheless, we do not attempt to model and subtract them. Instead, we will derive conservative constraints requiring

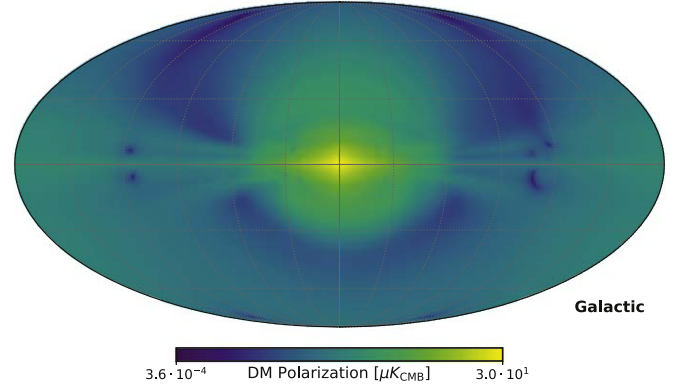


Figure 18. Example morphology of the DM synchrotron Polarization amplitude at 30 GHz for $m_{\text{DM}} = 50$ GeV annihilating in $\mu^+\mu^-$ pairs with a thermal cross section and the Psh+11 GMF model.

that the DM signal does not exceed the observed intensity or level of polarization.

We consider WIMPs in the mass range between 5 GeV and 1 TeV for annihilation into three representative channels: $\tau^+\tau^-$ and $\mu^+\mu^-$, producing a hard e^\pm spectrum, and $b\bar{b}$, giving a softer spectrum. To propagate the e^\pm in the Galaxy and derive the all-sky synchrotron maps from DM annihilations, we use GALPROP code version v54r2766³⁴ as adapted in Egorov et al. (2016).³⁵

The main systematic uncertainty of the analysis is expected to come from the modeling of the GMF because it is not well constrained (Jaffe 2019). The GMF is known to have at least two components: an isotropic turbulent, random field and a large-scale regular one. To gauge the uncertainties related to the GMF, we consider the following three models: The Sun +10 model (Sun et al. 2008; Sun & Reich 2010), the Psh+11 model (Pshirkov et al. 2011), and the JF12 model proposed by Jansson & Farrar (2012a, 2012b). These three models differ in both the regular and the random MF components. It is important to note that the intensity and polarization signal depend differently on the MF properties. Specifically, while the intensity depends on the total (random+ordered) MF strength, polarization only depends on the regular component of the field.

We show in Figure 18 an example of the morphology of the synchrotron polarization amplitude from DM at 30 GHz for $m_{\text{DM}} = 50$ GeV annihilating in $\mu^+\mu^-$ pairs with a thermal cross section and for the Psh+11 GMF model. For each DM mass and annihilation channel, we compute the DM intensity and polarization map and derive upper bounds on the annihilation cross section by requiring that the DM emission does not exceed the observed Planck signal plus the error estimated

³⁴ Publicly available at <https://gitlab.mpcdf.mpg.de/aws/galprop>.

³⁵ Publicly available at https://github.com/a-egorov/GALPROP_DM.

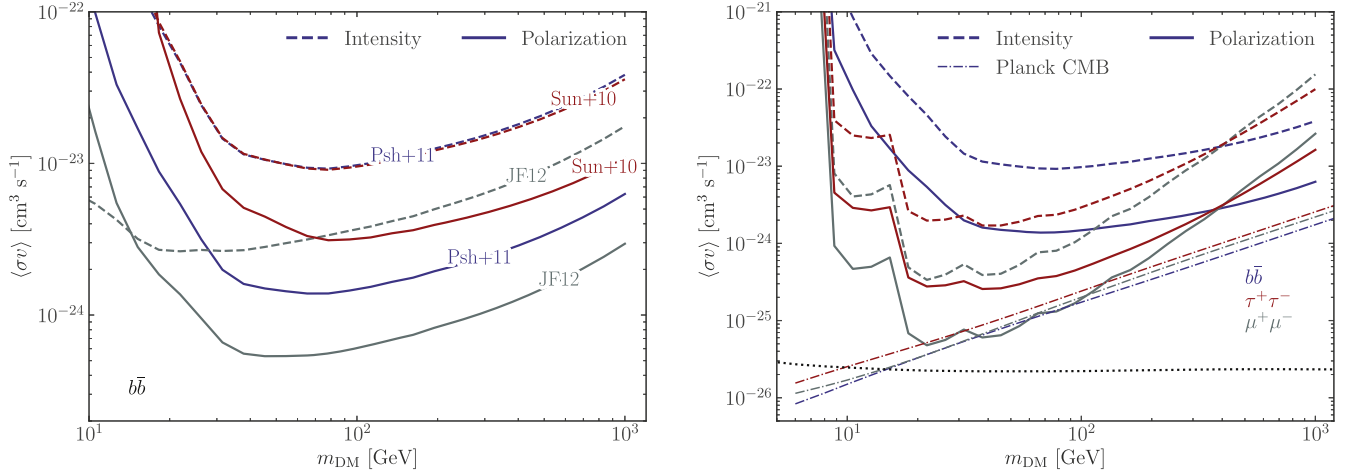


Figure 19. Upper limits on the DM annihilation cross section from the intensity and polarization data at 30 GHz. Left: effect of the GMF modeling for the $\bar{b}b$ channel. Right: constraints for different annihilation channels for the Psh+11 GMF. Also shown for comparison are the constraints obtained from Planck CMB data (Aghanim et al. 2020b).

before. The final quoted upper limits are given by the most constraining pixel.

The DM constraints obtained for the $\bar{b}b$ channel for intensity and polarization are illustrated in Figure 19 (left) for different GMF models. This illustrates the main result of the analysis, namely the fact that polarization limits are about a factor of 10 more constraining than the ones derived from intensity maps. As expected, however, the GMF provides a significant uncertainty also of about one order of magnitude. Nonetheless, polarization is always more constraining than intensity, independently of the GMF model. Further systematic uncertainties related to the choice of the propagation setup or the DM radial profile are discussed in Manconi et al. (2022).

The upper limits for the three annihilation channels considered are shown in Figure 19 (right) for a fixed choice of Psh+11 GMF. For the $\mu^+\mu^-$ channel, the polarization upper limits at several tens of GeV are close to the thermal relic value (Steigman et al. 2012) and competitive with Planck CMB constraints (Aghanim et al. 2020b).

The stronger DM constraints from polarization come mainly from two effects. First, the observed intensity and polarization emissions have significantly different morphologies, with polarization presenting filaments, or arms, and leaving interarm regions with low background very close to the Galactic center, where the DM signal is highest. On the contrary, the observed intensity is quite uniform and the S/N for DM peaks farther away from the Galactic center. Second, polarization presents a lower overall background level.

In summary, we have derived, for the first time, limits on the DM annihilation cross section from Planck observations of the polarized synchrotron emission, finding constraints about one order of magnitude stronger than the ones derived from intensity. The constraints can be further improved by proper

modeling and removal of the astrophysical synchrotron signal. We leave this assessment to future work.

5. Discussion

A main consensus of the workshop was that there are encouraging prospects for near-term analysis projects related to both (i) the radio SZ effect (discussed in Section 4.9) and (ii) cross-correlation analyses. These may either not require much in the way of new observations or may require new observations that are feasible in scope.

As discussed in Section 4.9 a positive detection of the radio SZ effect would confirm the RSB as extragalactic. Additionally, redshift tomography would be possible by utilizing clusters of different redshifts, allowing a potential constraint to the redshift of origin of the RSB. There may already be sufficient radio observations of clusters in the literature from LOFAR and/or MeerKAT. In the case of LOFAR, where the radio SZ effect would manifest as an increase in emission, which would have to be separated from emission due to sources in a cluster itself, these could be targeted observations of clusters (e.g., Savini et al. 2019) or clusters surreptitiously seen in surveys such as the LOFAR Two-meter Sky Survey (LoTSS—Shimwell et al. 2017). In the case of MeerKAT, the MeerKAT Cluster Legacy Survey (MGCLS—Knowles et al. 2022) has detected over 100 clusters at $8''$ resolution in the L band (900–1670 MHz), where the radio SZ effect would manifest as a decrement.

For cross-correlation analyses, in addition to the observations of Offringa et al. (2022) discussed in Section 4.3, there are also legacy LOFAR observations of other fields and the possibility of targeting additional fields. These radio observations could be cross-correlated with available maps at other

wavelengths, which trace distinct structures in the universe. These include CMB lensing (e.g., Planck—Aghanim et al. 2020c), which traces the overall matter distribution; catalogs in the optical, which trace the galaxy distribution; and X-rays, which trace the black hole distribution. The latter is important for potentially constraining PBH origin scenarios such as in Sections 4.13 and 4.14.

Another consensus of the workshop was that the 310 MHz absolute map project discussed in Sections 4.1.1 and 4.2 should be prioritized over the other potential measurements discussed at the first RSB workshop. These other proposed measurements were (i) a targeted one at 120 MHz and (ii) a measurement in the gigahertz range with greater sky coverage than ARCADE 2. However, we did agree that a future measurement to determine whether the synchrotron spectrum hardens at frequencies >10 GHz would be valuable, in particular for discriminating between various proposed origin scenarios for the RSB. Such a measurement would likely require a future space mission, although the Tenerife Microwave Spectrometer (TMS—Paz et al. 2020) may prove useful in this regard.

We also discussed the need to understand more about the small-scale structure of the Galactic magnetic field, which is necessary for investigations that use the observed polarization information to constrain a potential Galactic origin for the RSB such as in Section 4.16. There are already comprehensive maps of Faraday rotation in the literature (e.g., Oppermann et al. 2012), which cannot be explained with current models of the Galactic magnetic field, so larger-scale models of the Galactic magnetic field are necessary. We look forward to the publication of polarization maps from C-BASS (discussed in Sections 4.7 and 4.6) and the Australia Square Kilometer Array Pathfinder (ASKAP) polarization Sky Survey of the Universe’s Magnetism (POSSUM—e.g., Andreson et al. 2021).

Another point raised, which was also emphasized at the first RSB workshop, is that proposed origin scenarios should be testable with observations. These observations could potentially be in the radio and/or some other wave band(s), at any angular scale(s), in intensity and/or polarization, and either new or available in the literature.

The workshop and its format were unanimously declared a success by the participants, and, along with the consensus on the issues discussed above, there was agreement on the importance of the topic and of another dedicated meeting in the time span of 4–5 yr.

We thank the INFN and University of Torino for the financial support to the meeting, and the Hotel Barolo and Brezza restaurant and winery for their hospitality. J.S. acknowledges support from a University of Richmond College of Arts and Sciences Sabbatical Fellowship. M.R. and E.T. acknowledge funding from PRIN research grant No.

20179P3PKJ and the “Department of Excellence” grant funded by MIUR, and from the research grant TAsP funded by INFN. S.H. acknowledges support from NSF grant No. PHY-1914409. E.P. acknowledges the support from the Ministero degli Affari Esteri della Cooperazione Internazionale—Direzione Generale per la Promozione del Sistema Paese Progetto di Grande Rilevanza ZA18GR02. C.H. acknowledges support from the Leverhulme Trust through an Early Career Research Fellowship.

ORCID iDs

J. Singal  <https://orcid.org/0000-0001-5436-8503>
 I. P. Carucci  <https://orcid.org/0000-0001-5287-0065>
 C. DiLullo  <https://orcid.org/0000-0001-5944-9118>
 J. P. Leahy  <https://orcid.org/0000-0003-2514-9592>
 S. Mittal  <https://orcid.org/0000-0002-0247-618X>
 R. A. Monsalve  <https://orcid.org/0000-0002-3287-2327>
 G. Piccirilli  <https://orcid.org/0000-0002-3341-1872>

References

- Abazajian, K., Addison, G., Adshead, P., et al. 2019, arXiv:1907.04473
 Abdalla, E., Ferreira, E., Landim, R., et al. 2022, *A&A*, 664, A14
 Abdurashidova, Z., Aguirre, J., Alexander, P., et al. 2022, *ApJ*, 925, 221
 Acharya, S. K., & Chluba, J. 2022, *MNRAS*, 515, 5775
 Acharya, S. K., & Chluba, J. 2023, *MNRAS*, 519, 2138
 Ackermann, M., Ajello, M., Albert, A., et al. 2012, *PhRvD*, 85, 083007
 Ackermann, M., Ajello, M., Albert, A., et al. 2015, *ApJ*, 799, 86
 Ackermann, M., Ajello, M., Baldini, L., et al. 2018, *PhRvL*, 121, 241101
 Adam, R., Ade, P., Aghanim, N., et al. 2016, *A&A*, 594, A10
 Ade, P., Aghanim, N., Arnaud, M., et al. 2011, *A&A*, 536, A18
 Ade, P., Aguirre, J., Ahmed, Z., et al. 2019, *JCAP*, 2019, 056
 Aghanim, N., Akrami, Y., Arroja, F., et al. 2020a, *A&A*, 641, A1
 Aghanim, N., Akrami, Y., Ashdown, M., et al. 2020b, *A&A*, 641, A6
 Aghanim, N., Akrami, Y., Ashdown, M., et al. 2020c, *A&A*, 641, A8
 Aguilar, M., Ali Cavazonza, L., Alpat, B., et al. 2019, *PhRvL*, 122, 101101
 Akrami, Y., Ashdown, M., Aumont, J., et al. 2020, *A&A*, 641, A4
 Albert, J., Anderson, B., Bechtol, K., et al. 2017, *ApJ*, 834, 110
 Alonso, D., Bellini, E., Hale, C., Jarvis, M., & Schwarz, D. 2021, *MNRAS*, 502, 876
 Alonso, D., Ferreira, P., & Santos, M. 2014, *MNRAS*, 444, 3183
 Alvarez, H., Aparici, J., May, J., & Olmos, F. 1999, *A&AS*, 124, 315
 Alves, M. I. R., Boulanger, F., Ferrière, K., et al. 2018, *A&A*, 611, L5
 Amiri, M., Bandura, K., Anja, B., et al. 2022, *ApJ*, 932, 100
 Andersson, B.-G., & Potter, S. B. 2006, *ApJL*, 640, L51
 André, P., Baccigalupi, C., Banday, A., et al. 2014, *JCAP*, 2014, 006
 Andreson, C., Heald, G., Eilek, J., et al. 2021, *PASA*, 38, 20A
 Bacon, D., Battye, R., Bull, P., et al. 2020, *PASA*, 37, e007
 Barkana, R. 2016, *PhR*, 645, 1
 Barry, N., Bernardi, G., Greig, B., Kern, N., & Mertens, F. 2022, *JATIS*, 8, 1007
 Battistelli, E., Govoni, F., Murgia, M., et al. 2019, *BAAS*, 51, 208
 Begelman, M. C., Blandford, R. D., & Rees, M. J. 1984, *RvMP*, 56, 255
 Bell, A. R. 1978a, *MNRAS*, 182, 147
 Bell, A. R. 1978b, *MNRAS*, 182, 443
 Benthem, P., Wayth, R., de Lera Acedo, E., et al. 2021, *A&A*, 655, 5
 Berdyugin, A., Piirola, V., & Teerikorpi, P. 2014, *A&A*, 561, A24
 Bernardi, G., McQuinn, M., & Greenhill, L. 2015, *ApJ*, 799, 90
 Bernardi, G., de Bruyn, A., Harker, G., et al. 2010, *A&A*, 522, 67
 Bernardi, G., Greenhill, L., Mitchell, D., et al. 2013, *ApJ*, 771, 105
 Bernardi, G., Zwart, J. T. L., Price, D., et al. 2016, *MNRAS*, 461, 2847
 Bersanelli, M., Bensadoun, M., De Amici, G., et al. 1994, *ApJ*, 424, 517
 Beuermann, K., Kanbach, G., & Berkhuisen, E. M. 1985, *A&A*, 153, 17

- Bevins, H., de Lera Acedo, E., Fialkov, A., et al. 2022, *MNRAS*, **513**, 4507
- Bevins, H. T. J., Heimersheim, S., Abril-Cabezas, I., et al. 2023, arXiv:2301.03298
- Biermann, P., Nath, B., Caramete, L., et al. 2014, *MNRAS*, **441**, 1147
- Bobin, J., Starck, J., Fadili, J., Moudden, Y., & Donoho, D. 2007, *ITIP*, **16**, 2675
- Bobin, J., Sureau, F., Starck, J., Rassat, A., & Paykari, P. 2014, *A&A*, **563**, A105
- Bolliet, B., Chluba, J., & Battye, R. 2021, *MNRAS*, **507**, 3148
- Bonaldi, A., Bonato, M., Galluzzi, V., et al. 2018, *MNRAS*, **482**, 1
- Bonaldi, A., Bonato, M., Galluzzi, V., et al. 2019, *MNRAS*, **482**, 2
- Booth, R., de Blok, W., Jonas, J., & Fanaroff, B. 2009, arXiv:0910.2935
- Bowman, J. D., Rogers, A. E. E., Monsalve, R. A., Mozdzen, T. J., & Mahesh, N. 2018, *Natur*, **555**, 67
- Brandenburg, A., Kahniashvili, T., & Tevzadze, A. G. 2015, *PhRvL*, **114**, 075001
- Breitschwerdt, D., & de Avillez, M. A. 2006, *A&A*, **452**, L1
- Breitschwerdt, D., Feige, J., Schulreich, M. M., et al. 2016, *Natur*, **532**, 73
- Bridle, A. 1967, *MNRAS*, **136**, 219
- Broderick, A., Pfrommer, C., Puchwein, E., Chang, P., & Smith, K. 2014, *ApJ*, **796**, 12
- Bryan, G. L., Norman, M., O'Shea, B., et al. 2014, *ApJS*, **211**, 19
- Bull, P., Ferreira, P. G., Patel, P., & Santos, M. G. 2015, *ApJ*, **803**, 21
- Burigana, C., Danese, L., & de Zotti, G. 1991, *A&A*, **246**, 49
- Bykov, A. M., Petrov, A. E., Krassilchtchikov, A. M., et al. 2019, *ApJL*, **876**, L8
- Byrne, R., Morales, M., Hazelton, B., et al. 2022, *MNRAS*, **510**, 2011
- Cappelluti, N., Hasinger, G., & Natarajan, P. 2022, *ApJ*, **926**, 205
- Caputo, A., Liu, H., Mishra-Sharma, S., Pospelov, M., & Ruderman, J. 2022, arXiv:2206.07713
- Caputo, A., Liu, H., Mishra-Sharma, S., & Ruderman, J. 2020, *PhRvL*, **125**, 221303
- Carr, B., & Kuhnel, F. 2022, *ScPPL*, 48
- Carr, B., & Sakellariadou, M. 1999, *ApJ*, **516**, 195
- Carretti, E., Haverkorn, M., Staveley-Smith, L., et al. 2019, *MNRAS*, **489**, 2330
- Carucci, I., Irfan, M., & Bobin, J. 2020, *MNRAS*, **499**, 304
- Chang, T., Pen, U., Bandura, K., & Peterson, J. 2010, *Natur*, **466**, 463
- Chluba, J. 2013, *MNRAS*, **434**, 352
- Chluba, J. 2015, *MNRAS*, **454**, 4182
- Chluba, J., Abitbol, M. H., Aghanim, N., et al. 2021, *ExA*, **51**, 1515
- Chluba, J., & Ali-Haïmoud, Y. 2016, *MNRAS*, **456**, 3494
- Chluba, J., Kogut, A., Patil, S. P., et al. 2019, *BAAS*, **51**, 184
- Chluba, J., & Sunyaev, R. A. 2012, *MNRAS*, **419**, 1294
- Christensson, M., Hindmarsh, M., & Brandenburg, A. 2001, *PhRvE*, **64**, 056405
- Cirelli, M., & Taoso, M. 2016, *JCAP*, **07**, 041
- Cline, J., & Vincent, A. 2014, *JCAP*, **02**, 011C
- Collins, D. C., Xu, H., Norman, M., et al. 2010, *ApJS*, **186**, 308
- Condon, J., Cotton, W., Fomalont, E., et al. 2012, *ApJ*, **758**, 23
- Condon, J., Cotton, W., Greisen, E., et al. 1998, *AJ*, **115**, 5
- Cook, J. H., Trott, C. M., & Line, L. J. B. 2022, *MNRAS*, **514**, 790
- Cooray, A., & Sheth, R. 2002, *PhRvL*, **372**, 1
- Costain, C. 1960, *MNRAS*, **120**, 248
- Cox, D. P., & Reynolds, R. J. 1987, *ARA&A*, **25**, 303
- Crichton, D., Aich, M., Amara, A., et al. 2022, *JATIS*, **8**, 011019
- Cummings, A. C., Stone, E. C., Heikkilä, B. C., et al. 2016, *ApJ*, **831**, 18
- Cunnington, S., Li, Y., Santos, M. G., et al. 2023, *MNRAS*, **518**, 6262
- Delahaye, T., Boehm, C., & Silk, J. 2012, *MNRAS*, **422**, L16
- Dillon, J. S., Neben, A., Hewitt, J., et al. 2015, *PhRvD*, **91**, 3011
- Dolfi, A., Branchini, E., Bilicki, M., et al. 2019, *A&A*, **623**, A148
- Dowell, J., Taylor, G., Schnizel, F., Kassim, N., & Stoval, K. 2017, *MNRAS*, **469**, 4
- Dowell, J., & Taylor, G. B. 2018, *ApJL*, **858**, 9
- Dowell, J., Wood, D., Stovall, K., et al. 2012, *JAI*, **1**, 1250006
- Draper, A., Northcott, S., & Ballantyne, D. 2011, *ApJL*, **741**, L39
- Dubrovich, V. K. 1975, *SvAL*, **1**, 196
- Dyson, T., Chiang, H. C., Egan, E., et al. 2021, *J. Astron. Instrum.*, **10**, 2150007
- Egorov, A., Gaskins, J., Pierpaoli, E., & Pietrobon, D. 2016, *JCAP*, **03**, 060
- Ewall-Wice, A., Chang, T., Lazio, J., et al. 2018, *ApJ*, **868**, 63
- Ewall-Wice, A., Dillon, J. S., Hewitt, J., et al. 2016, *MNRAS*, **460**, 4320
- Fang, K., & Linden, T. 2015, *PhRvD*, **91**, 083501
- Fang, K., & Linden, T. 2016, *JCAP*, **10**, 004
- Feng, C., & Holder, G. 2018, *ApJL*, **858**, L17
- Ferramacho, L., Santos, M., Jarvis, M., & Camera, S. 2014, *MNRAS*, **442**, 2511
- Fialkov, A., & Barkana, R. 2019, *MNRAS*, **486**, 1763
- Fialkov, A., Barkana, R., & Visbal, E. 2014, *Natur*, **506**, 197
- Field, G. 1958, *Proc. IRE*, **46**, 240
- Fixsen, D. J., Cheng, E. S., Gales, J. M., et al. 1996, *ApJ*, **473**, 576
- Fixsen, D., Kogut, A., Levis, S., et al. 2011, *ApJ*, **734**, 5
- Fornasa, M., & Sanchez-Conde, M. A. 2015, *PhR*, **598**, 1
- Fornengo, N., Lineros, R., Regis, M., & Taoso, M. 2011, *PhRvL*, **107**, 271302
- Fornengo, N., Lineros, R., Regis, M., & Taoso, M. 2014, *JCAP*, **04**, 008
- Fortes, E., Miranda, O., Stecker, F., & Wuensche, C. 2019, *JCAP*, **11**, 047
- Franzen, T., Jackson, C., Offringa, A., et al. 2015, *PhR*, **598**, 1
- Frisch, P. C., Berdyugin, A., Piirola, V., et al. 2015, *ApJ*, **814**, 112
- Furlanetto, S., Oh, P., & Briggs, F. 2006, *PhR*, **433**, 181
- Garsden, H., Greenhill, H., Bernardi, G., et al. 2021, *MNRAS*, **506**, 5802
- George, E., Reichardt, C., Aird, K., et al. 2015, *ApJ*, **799**, 177
- Gervasi, M., Tartari, A., Zannoni, M., Boella, G., & Sironi, G. 2008, *ApJ*, **682**, 223
- Ghosh, A., Mertens, F., Bernardi, G., et al. 2020, *MNRAS*, **495**, 2813
- Górski, K. M., Hivon, E., Banday, A. J., et al. 2005, *ApJ*, **622**, 759
- Gry, C., & Jenkins, E. B. 2017, *A&A*, **598**, A31
- Guzmán, A. E., May, J., Alvarez, H., & Maeda, K. 2011, *A&A*, **525**, A138
- Guzman, J., Whiting, M., Voronkov, M., et al. 2019, ASKAPsoft: ASKAP science data processor software, Astrophysics Source Code Library, ascl:1912.003
- Hale, C., McConnell, D., Thompson, A., et al. 2021, *PASA*, **38**, e058
- Hardcastle, M., Shimwell, T., Tasse, C., et al. 2021, *A&A*, **648**, 10
- Hart, L., & Chluba, J. 2023, *MNRAS*, **519**, 3664
- Hart, L., Roti, A., & Chluba, J. 2020, *MNRAS*, **497**, 4535
- Hasinger, G. 2020, *JCAP*, **2020**, 022
- Haslam, C., Salter, C., Stoffel, H., & Wilson, W. 1982, *A&AS*, **47**, 1
- Hazumi, M., Ade, P. A. R., Adler, A., et al. 2020, *Proc. SPIE*, **11443**, 114432F
- Heesen, V., Brinks, E., Krause, M. G. H., et al. 2015, *MNRAS*, **447**, L1
- Herrera Ruiz, N., Middelberg, E., Deller, A., et al. 2017, *A&A*, **607**, A132
- Hicks, B. C., Paravastu-Dalal, N., Stewart, K., et al. 2012, *PASP*, **124**, 1090
- Hills, R., Kulkarni, G., Meerburg, G., & Pichwein, D. 2018, *Natur*, **564**, E32
- Holder, G. 2014, *ApJ*, **780**, 112
- Holder, G., & Chluba, J. 2022, arXiv:2110.08373
- Holler, C. M., Taylor, A. C., Jones, M. E., et al. 2013, *ITAP*, **61**, 117
- Hooper, D., Belikov, A., Jeltema, T., et al. 2012, *PhRvD*, **863**, 003H
- Hotan, A. W., Bunton, J. D., Chippendale, A. P., et al. 2021, *PASA*, **38**, e009
- Hotan, A. W., Bunton, J. D., Harvey-Smith, L., et al. 2014, *PASA*, **31**, e041
- Howell, T., & Shakeshaft, J. 1966, *Natur*, **210**, 1318
- Hu, W., & Silk, J. 1993, *PhRvL*, **70**, 2661
- Hutschenreuter, S., Anderson, C. S., Betti, S., et al. 2022, *A&A*, **657**, A43
- Intema, H., Jagannathan, P., Mooley, K., & Frail, D. 2017, *A&A*, **598**, A78
- Irfan, M. O., Bull, P., Santos, M. G., et al. 2022, *MNRAS*, **509**, 4923
- Iverson, R., Alexander, D., Biggs, A., et al. 2010a, *MNRAS*, **402**, 245
- Iverson, R., Magnelli, B., Ibar, E., et al. 2010b, *A&A*, **518**, L31
- Jaffe, T. 2019, *Galax*, **7**, 52
- Jansson, R., & Farrar, G. 2012a, *ApJ*, **757**, 14
- Jansson, R., & Farrar, G. 2012b, *ApJL*, **761**, L11
- Johnston, S., Bailes, M., Bartel, N., et al. 2007, *PASA*, **24**, 174
- Jonas, J., Baart, E., & Nicolson, G. 1998, *MNRAS*, **297**, 997
- Jonas, J. L. 2009, *Proc. IEEE*, **97**, 1522
- Jonas, J. L. 2016, in Proc. MeerKAT Science: On the Pathway to the SKA, ed. A. R. Taylor, F. Camilo, & L. Leeuw (Stellenbosch, South Africa: Proc. Sci.)
- Jones, M. E., Taylor, A. C., Aich, M., et al. 2018, *MNRAS*, **480**, 3224
- Joseph, T., Filipović, M. D., Crawford, E., et al. 2019, *MNRAS*, **490**, 1202
- Kerrigan, J. R., Pober, J., Ali, Z., et al. 2018, *ApJ*, **864**, 131
- Khatri, R., & Sunyaev, R. A. 2012, *JCAP*, **2012**, 016
- Knowles, K., Cotton, W., Rudnick, L., et al. 2022, *A&A*, **657**, A56
- Kogut, A., Fixsen, D., Levin, S., et al. 2011a, *ApJ*, **734**, 4
- Kogut, A., Fixsen, D., Chuss, D., et al. 2011b, *JCAP*, **07**, 025

- Krause, M., Diehl, R., Böhringer, H., et al. 2014, *A&A*, **566**, A94
- Krause, M., Fierlinger, K., Diehl, R., et al. 2013, *A&A*, **550**, A49
- Krause, M. G. H., & Hardcastle, M. J. 2021, *MNRAS*, **502**, 2807
- Kriele, M. A., Wayth, R. B., Bentum, M. J., Juswardy, B., & Trott, C. M. 2022, *PASA*, **39**, e017
- Lallement, R., Vergely, J.-L., Valette, B., et al. 2014, *A&A*, **561**, A91
- Landecker, T. L., & Wielebinski, R. 1970, *AuJPA*, **16**, 1
- Lawson, K., & Zhitnitsky, A. 2013, *PhLB*, **724**, 17
- Leclercq, I. A. 2017, PhD thesis, Univ. Manchester
- Lee, E., Chluba, J., & Holder, G. 2022, *MNRAS*, **512**, 5153
- Linsky, J. L., Redfield, S., & Tilipman, D. 2019, *ApJ*, **886**, 41
- López-Coto, R., Parsons, R. D., Hinton, J. A., et al. 2018, *PhRvL*, **121**, 251106
- Macario, G., Pupillo, G., Bernardi, G., et al. 2022, *JATIS*, **8**, 1014
- Maeda, K., Alvarez, H., Aparici, J., May, J., & Reich, P. 1999, *A&A*, **140**, 145
- Magnelli, B., Ivison, R., Lutz, D., et al. 2015, *A&A*, **573**, A45
- Manconi, S., Cuoco, A., & Lesgourgues, J. 2022, *PhRvL*, **129**, 111103
- Masui, K., Switzer, E., Banavar, N., et al. 2013, *ApJL*, **763**, L20
- Mather, J. C., Cheng, E. S., Cottingham, D. A., et al. 1994, *ApJ*, **420**, 439
- Matthews, A. M., Condon, J. J., Cotton, W. D., & Mauch, T. 2021, *ApJ*, **914**, 126
- McComas, D. J., Funsten, H. O., Fuselier, S. A., et al. 2011, *GeoRL*, **38**, L18101
- Mertens, F., Mevius, M., Koopmans, L., et al. 2020, *MNRAS*, **493**, 1662
- Mesinger, A. 2019, *The Cosmic 21-cm Revolution: Charting the First Billion Years of Our Universe* (Bristol: Institute of Physics Publishing)
- Mirabel, I., & Rodriguez, L. 2022, *NewAR*, **94**, 101642
- Mirocha, J., & Furlanetto, S. 2018, *MNRAS*, **483**, 1980
- Mittal, S., & Kulkarni, G. 2020, *MNRAS*, **510**, 4992
- Mittal, S., & Kulkarni, G. 2022a, *MNRAS*, **503**, 4264
- Mittal, S., & Kulkarni, G. 2022b, *MNRAS*, **515**, 2901
- Mittal, S., Ray, A., Kulkarni, G., & Dasgupta, G. 2022, *JCAP*, **2022**, 030
- Mondal, R., Fialkov, A., & Fling, C., et al. 2020, *MNRAS*, **498**, 4178
- Monsalve, R. A., Rogers, A. E. E., Bowman, J. D., et al. 2021, *ApJ*, **908**, 145
- Morabito, L., Jackson, N., Mooney, S., et al. 2022, *A&A*, **658**, A1
- Mozden, T. J., Bowman, J. D., Monsalve, R. A., & Rogers, A. E. E. 2016, *MNRAS*, **455**, 3890
- Mozden, T. J., Bowman, J. D., Monsalve, R. A., & Rogers, A. E. E. 2017, *MNRAS*, **464**, 4995
- Mozden, T. J., Mahesh, N., Monsalve, R. A., Bowman, J. D., & Rogers, A. E. E. 2019, *MNRAS*, **483**, 4411
- Murgia, M., Govoni, F., Feretti, L., et al. 2004, *A&A*, **424**, 429
- Murphy, E., Bolatto, A., Chatterjee, S., et al. 2018, in *ASP Conf. Ser. 517* (San Francisco, CA: ASP), **3**
- Murphy, E., & Chary, R. 2018, *ApJ*, **861**, 27
- Muxlow, T. W. B., Thomson, A. P., Radcliffe, A. P., et al. 2018, *MNRAS*, **495**, 1188
- Natwariya, P. 2021, *EPJC*, **81**, 394
- Negrello, M., Magliocchetti, M., & De Zotti, G. 2006, *MNRAS*, **368**, 935
- Nusser, A., & Tiwari, P. 2015, *AJ*, **812**, 85
- Offringa, A., Singal, J., Heston, S., Horiuchi, S., & Lucero, L. 2022, *MNRAS*, **509**, 114
- Oppermann, N., Junkelwitz, H., Robbers, G., et al. 2012, *A&A*, **542**, A93
- Patil, A., Yatawatta, S., Koopmans, L., et al. 2017, *ApJ*, **838**, 65
- Pauliny-Toth, I., & Shakeshaft, J. 1962, *MNRAS*, **124**, 61
- Paz, A., Rubiño-Martín, J., Hoyland, R., et al. 2020, *Proc. SPIE*, **11447**, 114476N
- Peebles, P. J. E. 2022, *AnPhy*, **447**, 169159
- Pelgrims, V., Ferrière, K., Boulanger, F., et al. 2020, *A&A*, **636**, A17
- Phillips, S., Kearsy, S., Osborne, J., Haslam, C., & Stoffel, H. 1981, *A&A*, **103**, 405
- Piccirilli, G., Migliaccio, M., Branchini, E., & Dolfi, A. 2022, arXiv:2208.07774
- Picquetot, A., Acero, F., Bobin, J., et al. 2019, *A&A*, **627**, A139
- Pirola, V., Berdyugin, A., Frisch, P. C., et al. 2020, *A&A*, **635**, A46
- Pinetti, E., Camera, S., Fornengo, N., & Regis, M. 2020, *JCAP*, **2020**, 044
- Ponente, P., Ascasibar, Y., & Diego, J. 2011, *MNRAS*, **419**, 691
- Pospelov, M., Pradler, J., Ruderman, J. T., & Urbano, A. 2018, *PhRvL*, **121**, 031103
- Price, D. C., Greenhill, L. J., Fialkov, A., et al. 2018, *MNRAS*, **478**, 4193
- Pshirkov, M., Tinyakov, P., Kronberg, P., & Newton-McGee, K. 2011, *ApJ*, **738**, 192
- Raimundo, S. I., & Fabian, A. C. 2009, *MNRAS*, **396**, 1217
- Redfield, S., & Linsky, J. L. 2008, *ApJ*, **673**, 283
- Redfield, S., & Linsky, J. L. 2015, *ApJ*, **812**, 125
- Reich, P., & Reich, W. 1986, *A&A*, **63**, 205
- Reis, I., Fialkov, A., & Barkana, R. 2020a, *MNRAS*, **499**, 5993
- Reis, I., Fialkov, A., & Barkana, R. 2020b, *MNRAS*, **506**, 5479
- Roger, R., Costain, C., Landecker, T., & Swerdlyk, C. 1999, *A&A*, **137**, 7
- Rogers, A. E. E., & Bowman, J. D. 2008, *AJ*, **136**, 641
- Rybicki, G. B., & Lightman, A. P. 1979, *Radiative Processes in Astrophysics* (New York: Wiley-VCH)
- Savini, F., Brügger, M., Rafferty, D., et al. 2019, *A&A*, **622**, A24
- Scheuer, P. A. G. 1957, *PCPS*, **53**, 764
- Schulreich, M., Breitschwerdt, D., Feige, J., et al. 2018, *Galax*, **6**, 26
- Seiffert, M., Fixsen, D., Kogut, A., et al. 2011, *ApJ*, **734**, 6
- Shankar, F., Weinberg, D. H., & Miralda-Escudé, J. 2008, *ApJ*, **690**, 20
- Shaw, J., Sigurdson, K., Sitwell, M., Stebbins, A., & Pen, U. 2015, *PhRvD*, **91**, 83514
- Shimwell, T., Röttering, H., Best, P., et al. 2017, *A&A*, **598**, A104
- Simon, T., Franco, G., Du, P., Poulin, V., & Tsai, Y. 2022, *Phys. Rev. D*, **106**, 023516
- Singal, J., Kogut, A., Jones, E., & Dunlap, H. 2015, *ApJL*, **799**, L10
- Singal, J., Stawarz, L., Lawrence, A., & Petrosian, V. 2010, *MNRAS*, **409**, 1172
- Singal, J., Fixsen, D., Kogut, A., et al. 2011, *ApJ*, **730**, 138
- Singal, J., Haider, J., Ajello, M., et al. 2018, *PASP*, **130**, 985
- Singh, S., & Subrahmanyan, R. 2019, *ApJ*, **880**, 26
- Singh, S., Subrahmanyan, R., Udaya Shankar, N., et al. 2018, *ApJ*, **858**, 54
- Singh, S., Jishnu, N., Subrahmanyan, R., et al. 2022, *NatAs*, **6**, 607
- Smolčić, V., Novak, M., Bondi, M., et al. 2017, *A&A*, **602**, A1
- Snowden, S. L., Chiao, M., Collier, M. R., et al. 2014, *ApJL*, **791**, L14
- Snowden, S. L., Egger, R., Finkbeiner, D. P., et al. 1998, *ApJ*, **493**, 715
- Snowden, S. L., Egger, R., Freyberg, M. J., et al. 1997, *ApJ*, **485**, 125
- Snowden, S. L., Heiles, C., Koutoumpa, D., et al. 2015, *ApJ*, **806**, 119
- Spinelli, M., Bernardi, G., Garsden, H., et al. 2021, *MNRAS*, **505**, 1575
- Spinelli, M., Carucci, I. P., Cunningham, S., et al. 2022, *MNRAS*, **509**, 2048
- Spolyar, D., Bodenheimer, P., Freese, K., & Gondolo, P. 2009, *ApJ*, **705**, 1031
- Steigman, G., Dasgupta, B., & Beacom, J. 2012, *PhRvD*, **86**, 023506
- Subrahmanyan, R., & Cowsik, R. 2013, *ApJ*, **776**, 42
- Sun, X., & Reich, W. 2010, *RAA*, **10**, 1287
- Sun, X. H., Reich, W., Waelkens, A., & Enßlin, T. A. 2008, *A&A*, **477**, 573
- Sunyaev, R. A., & Chluba, J. 2009, *AN*, **330**, 657
- Sunyaev, R. A., & Zeldovich, Y. B. 1970a, *Ap&SS*, **7**, 20
- Sunyaev, R. A., & Zeldovich, Y. B. 1970b, *CoASP*, **2**, 66
- Sunyaev, R. A., & Zeldovich, Y. B. 1980, *MNRAS*, **190**, 413
- Sur, S. 2019, *MNRAS*, **488**, 3439
- Sweijen, F., van Weeren, R. J., Röttgering, H. J. A., et al. 2022, *NatAs*, **6**, 350
- Switzer, E., Masui, K., Bandura, K., et al. 2013, *MNRAS*, **434**, L46
- Taylor, A. R., & Salter, C. J. 2010, in *ASP Conf. Ser. 438*, *The Dynamic Interstellar Medium: A Celebration of the Canadian Galactic Plane Survey*, ed. R. Kothés, T. L. Landecker, & A. G. Willis (San Francisco, CA: ASP), **402**
- Taylor, G. B., Ellingson, S. W., Kassim, N. E., et al. 2012, *JAI*, **1**, 1250004
- Tello, C., Villela, T., Torres, S., et al. 2013, *A&A*, **556**, 1
- Testori, J. C., Reich, P., & Reich, W. 2008, *A&A*, **484**, 733
- Thyagarajan, N., Jacobs, D., Bowman, J., et al. 2015, *ApJL*, **807**, L28
- Tribble, P. C. 1991, *MNRAS*, **250**, 726
- Trott, C., Jordan, C., Midgley, S., et al. 2020, *MNRAS*, **493**, 4711
- Turtle, A. J., & Baldwin, J. E. 1962, *MNRAS*, **124**, 297
- van Haarlem, M. R., Wise, M., Gunst, A., et al. 2013, *A&A*, **556**, 2
- Venumadhav, T., Dai, L., Kaurov, A., & Zaldarriaga, M. 2018, *PhRvD*, **98**, 103513
- Vernstrom, T., Gaensler, B., Brown, S., Lenc, E., & Norris, R. 2017, *MNRAS*, **467**, 4914
- Vernstrom, T., Scott, D., & Wall, J. 2011, *MNRAS*, **415**, 3641
- Vernstrom, T., Scott, D., Wall, J., et al. 2014, *MNRAS*, **440**, 2791
- Vidal, M., Dickinson, C., Davies, R. D., & Leahy, J. P. 2015, *MNRAS*, **452**, 656
- Vittino, A., Mertsch, P., Gast, H., et al. 2019, *PhRvD*, **100**, 043007

- Wallner, A., Feige, J., Kinoshita, N., et al. 2016, *Natur*, 532, 69
- Wang, J., Santos, M. G., Bull, P., et al. 2021, *MNRAS*, 505, 3698
- Wang, R., Wu, X.-B., & Kong, M.-Z. 2006, *ApJ*, 645, 890
- Weiland, J. L., Addison, G. E., Bennett, C. L., Halpern, M., & Hinshaw, G. 2022, *ApJ*, 936, 24
- Westerhout, G., & Oort, J. 1951, *BAN*, 11, 323
- Wilman, R., Miller, L., Jarvis, M., et al. 2008, *MNRAS*, 388, 1335
- Wollack, E. 1995, *RSci*, 66, 4305
- Wolleben, M., Landecker, T. L., Reich, W., & Wielebinski, R. 2006, *A&A*, 448, 411
- Wolz, L., Pourtsidou, A., Masui, K. W., et al. 2022, *MNRAS*, 510, 3495
- Wouthuysen, S. 1952, *AJ*, 57, 31
- Wu, F., Li, J., Zuo, S., et al. 2021, in 13th Int. Symp. on Antennas, Propagation and EM Theory (ISAPE), ed. Q. Chu, J. Wu, & R. Stone (Danvers, MA: IEEE), 1
- Wyatt, S. 1953, *ApJ*, 118, 304
- Xu, J., & Han, J. L. 2019, *MNRAS*, 486, 4275
- Yang, Y., Yang, G., Huang, X., Chen, X., & Zong, H. 2013, *PhRvD*, 87, 083519
- Yates, K. W., Wielebinski, R., & Landecker, T. L. 1967, *AJPh*, 20, 595
- Ysard, N., & Lagache, G. 2012, *A&A*, 547, A53
- Zucker, C., Goodman, A. A., Alves, J., et al. 2022, *Natur*, 601, 334
- Zwart, J., Santos, M., & Jarvis, M. 2015, *MNRAS*, 453, 1740